




Article

A Multidisciplinary Computational Framework for Topology Optimisation of Offshore Helidecks

Siamak Farajzadeh Khosroshahi ^{1,*} , Marinella Masina ², Alessandro Antonini ² , Edward Ransley ³ , James Mark William Brownjohn ⁴, Peter Dobson ⁵ and Dina D'Ayala ¹

¹ Department of Civil, Environmental and Geomatic Engineering, University College London, London WC1E 6BT, UK

² Faculty of Civil Engineering and Geosciences, Delft University of Technology, 2628 CN Delft, The Netherlands

³ School of Engineering, Computing and Mathematics, University of Plymouth, Plymouth PL4 8AA, UK

⁴ College of Engineering, Mathematics and Physical Sciences, University of Exeter, Exeter EX4 4QF, UK

⁵ Trinity House, Harwich CO12 3JW, UK

* Correspondence: s.khosroshahi@qmul.ac.uk

Abstract: Maintaining offshore steel structures is challenging and not environmentally friendly due to the frequent visits for inspection and repairs. Some offshore lighthouses are equipped with carbon steel helidecks fixed onto their lantern galleries in the 1970s to provide easy and safe access to maintenance staff and inspectors. Even though the helidecks supporting structures have maintained their integrity and are still functional in the offshore harsh environmental conditions, their inspection and maintenance remains a challenge due to the need of frequent visits which requires flying to the location of the lighthouse to bring the maintenance staff and equipment. We have developed a multidisciplinary computational framework to design new generation of aluminium helidecks for offshore lighthouses. We calculated the wind speed at the location of the Bishop Rock lighthouse based on the meteorological data, and the load distribution on the helideck due to such a wind condition, using computational fluid dynamic analysis. Then, we used the calculated wind load with other mechanical loads in the events of normal and emergency landings of a helicopter on this structure to find the best design configuration for this helideck. We generated a design space for different configurations of a beam structure and carried out, static, transient and buckling analysis to assess each case using finite element method. The selection criterion was set to find the structure with the minimum volume fraction and compliance while keeping the stress below the allowable stress. We found the structure with eight vertical and circumferential sections featuring two rows of diagonal bracing with one at the base and the other one at the third section from the base of the helideck was the optimum design for the considered loading in this work. This framework can be adopted for the design and optimisation of other offshore structures by other researchers and designers.

Keywords: lighthouse; topology optimisation; offshore; finite element analysis



Citation: Khosroshahi, S.F.; Masina, M.; Antonini, A.; Ransley, E.; Brownjohn, J.M.W.; Dobson, P.; D'Ayala, D. A Multidisciplinary Computational Framework for Topology Optimisation of Offshore Helidecks. *J. Mar. Sci. Eng.* **2022**, *10*, 1180. <https://doi.org/10.3390/jmse10091180>

Academic Editor: Carlos Guedes Soares

Received: 13 July 2022

Accepted: 17 August 2022

Published: 24 August 2022

Publisher's Note: MDPI stays neutral with regard to jurisdictional claims in published maps and institutional affiliations.



Copyright: © 2022 by the authors. Licensee MDPI, Basel, Switzerland. This article is an open access article distributed under the terms and conditions of the Creative Commons Attribution (CC BY) license (<https://creativecommons.org/licenses/by/4.0/>).

1. Introduction

Offshore lighthouses are architectural masterpieces shining for more than two centuries in seas around the British Isles [1,2]. Some of them were equipped with helidecks fixed onto their lantern galleries in the 1970s to provide easy and safe access to maintenance staff and inspectors. The helidecks supporting structures are made of carbon steels and take the form of linear elements connected by welds and bolts. Even though these helidecks have maintained their integrity and are still functional in the offshore harsh environmental conditions [3], thanks to frequent costly inspections and repairs, their 70s structural design underwent modest optimisation, due to the lack of computational methods available today [1,4]. This study adopts a multidisciplinary approach to develop a computational framework to design a new generation of light, robust and sustainable helidecks supporting structures for offshore lighthouses and thus reduce the carbon footprint of these structures.

Several computational methods are available to optimise the topology of structures, namely “density”, “level set”, “topological derivative”, “phase field” and “evolutionary”, each having their pros and cons [5]. These methods have been especially developed to be used in finite element (FE) models and several of them have been also implemented in commercial finite element software packages such as ANSYS, ABAQUS and Ls-Dyna [5–8]. These optimisation methods place the material in the design domain to obtain the best structural performance as a trade-off between maximum stiffness (minimum compliance) for minimum mass.

Even though the abovementioned methods have provided designers with powerful tools to optimise components under simple loading in a continuum domain [9–12], topology optimisation of beam/truss structures under multiple loadings, considering manufacturing constraints is not straightforward by means of the methods implemented in commercial software packages [13,14]. Thus, specific topology optimisation methods have been developed for beam and truss structures [15–17]. These methods are usually formulated based on a ‘ground structure’ approach [18], which is a network of joints distributed in the design space and connected by potential bars. The main objective of these methods is to find the coordinates of the joints and the cross-section area of linking bars to minimise the mass of the structure or to minimise its compliance [17]. Even though these methods are highly efficient for designing theoretically optimal lightweight structures, the solutions are usually complex in form and need simplifications to be feasible for fabrication [15]. Therefore, in this work we propose a computational framework to generate finite element models of possible configurations of beam structures for given dimensions adopted for lighthouse helidecks. Simulation under design loads for each possible configuration is carried out and a design space which represents the volume fraction of these configurations, and their compliance is generated. Then, we use this design space to find the best structure which has the minimum total mass and has the best performance under different loading scenarios, namely static load, buckling and time-dependent analyses.

Importantly, the design of these helidecks is substantially determined by the environmental loading conditions which are location-dependent for each lighthouse and affected by substantial uncertainty and variability. Therefore, we performed an extreme value analysis of maximum gust speed. Then we used the calculated maximum gust speed to carry out a computational fluid dynamic (CFD) analysis and calculated the pressure field around the helideck structure and lantern. Consequently, we defined the wind load on the helideck structure.

In the following section, the methods adopted for calculating the loads due to the extreme environmental conditions, the FE model validation and the computational framework for topology optimisation are described in detail. In Section 3, we present the results of our work and in Section 4 we discuss our findings and recommend directions for future works.

2. Methods

In the present work we focus on the development of a computational framework for the design of a helideck at the Bishop Rock lighthouse; however, the method and the framework developed here can be used for other lighthouses and perhaps for further offshore installations.

2.1. Bishop Rock Lighthouse Location

The Bishop Rock lighthouse is located off the southwest coast of England in the Celtic Sea at the geographical coordinates of 49° 52.3N and 6° 26.7W, as shown in Figure 1. The nearest meteorological station is located at Saint Mary’s airport in the Isles of Scilly (UK) which is almost 12 km northeast of the lighthouse.



Figure 1. (Left): The location of Bishop Rock lighthouse; (Right and top): Magnified view of “A” shown on the left figure; (Right and bottom): Magnified view of “B” shown on the right and top figure [Google Map].

2.2. The Current Helideck Structure on the Bishop Rock Lighthouse

The helideck structure is mounted on top of the lighthouse as shown in Figure 2. The total height of the lighthouse from the lowest point in its foundation to the mean focal plane of the lantern and the height of the helideck structure are 44.5 m and 6.4 m, respectively.

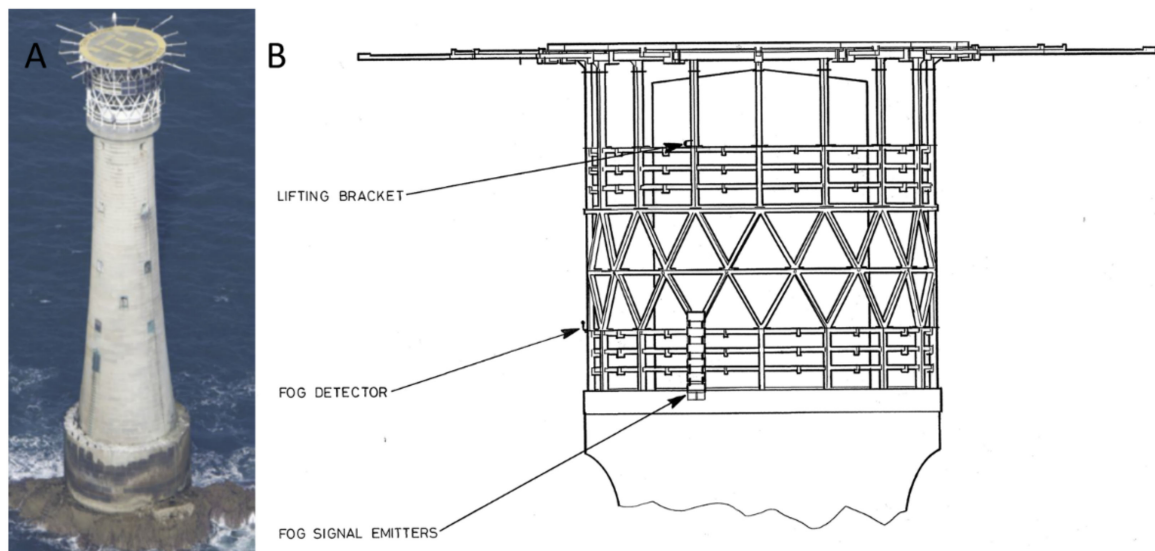


Figure 2. (A): Bishop Rock lighthouse (courtesy of Trinity House). (B): The helideck general assembly (courtesy of Trinity House).

The current helideck structure is made of carbon steel beams and boxes welded into subsections onshore and assembled using bolts and nuts on site. Some details of the current structure, including beams and joints, are shown in the drawing in Figure 3.

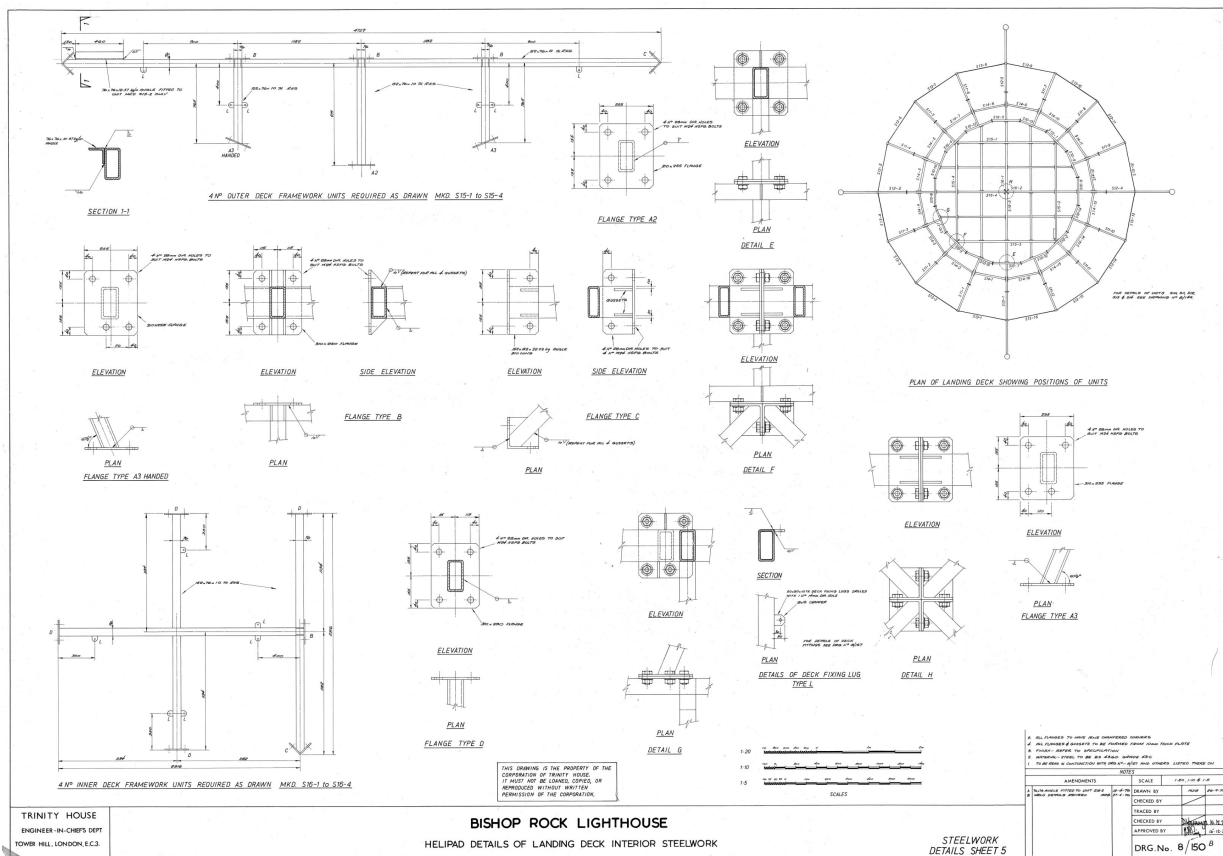


Figure 3. An example of detailed drawings of the current structure [courtesy of Trinity House].

The long exposure to the harsh offshore environmental condition caused severe corrosion on different areas of the helideck (see Figure 4) and regular inspection is planned to detect damages and repair the defected parts and sections. Due to the remote offshore locations of lighthouses, the maintenance of the helidecks is an expensive process. Therefore, for the design of the next generation of lighthouses' helidecks, we propose structures made of aluminium, which has substantially lower specific mass and high corrosion resistance.



Figure 4. Examples of corroded areas of the helideck [courtesy of Trinity House].

2.3. Extreme Value Analysis of Maximum Gust Speed

To determine the design wind load on the helideck structure at the top of the Bishop Rock lighthouse, the wind measurements collected at the Isles of Scilly were analysed. We extracted hourly mean wind speed and direction and maximum gust speed in an hour,

along with its direction and occurrence time, from the UK Met Office Integrated Data Archive System (MIDAS) Land and Marine Surface Stations Data (1853–current).

The dataset used in the study was obtained from the Centre for Environmental Data Analysis (CEDA) Archive [19] and it includes the measurements collected during the interval 1 January 1969–26 December 1981 at the historical Scilly/St Mary’s coast guard station (MIDAS station identifier 1385, WMO 03804), and the wind records of the period 21 October 1991–31 December 2020 at the Scilly/St Mary’s Airport station (MIDAS station identifier 1386, WMO 03803).

A Dines pressure tube anemometer was in use at the St Mary’s coast guard station with the vane at a height of 20 m above the ground and an estimated “effective height” of 17 m. A cup anemometer is used to measure the wind speed at the St Mary’s Airport station with the 3 s gust definition recommended by the World Meteorological Organization. As the wind is usually measured at a height of 10 m above ground by the UK operational network of surface stations, a standard height of 10 m was assumed for the cup anemometer at the St Mary’s Airport observing site in the Isles of Scilly.

2.3.1. Data Homogenisation

Hourly meteorological data of the Met Office MIDAS database have undergone a series of systematic quality control checks to ensure consistency of the observations [20]. Therefore, we only used the records flagged as quality checked by the Met Office in this work. Duplicate entries were removed by retaining only the most recent record. The dataset was then subjected to careful visual inspection and further standard quality checks to guarantee its accuracy.

A rather considerable shift is evident in the time series obtained by combining the raw gust speeds recorded by the historical coast guard station with those measured at St Mary’s airport after 21 October 1991. This shift is mainly due to the differences in the instrumentation employed at the two stations, observing practice, measurement height above the ground and specific characteristics of the observation site and its surroundings.

In the present work we followed the approach proposed in [21] to homogenise the gust data recorded at St Mary’s. By using the measured hourly mean wind speeds (\bar{U}) and the maximum gust speeds (\hat{u}) over the 1-h period, expected mean gust factor values were calculated for 16 cardinal directional sectors providing indirect indication on the turbulence intensity and the effective roughness length (z_0).

z_0 is, afterwards, used to derive directional correction factors for transforming the measured gust speeds to the standard conditions, i.e., 3 s gust, 10 m height, flat and open terrain with z_0 equal to 0.03 m.

We excluded hourly mean wind speeds (\bar{U}) lower than or equal to 5.5 m/s from our analysis to ensure that the atmospheric boundary layer can be treated as nearly neutral. To consider the response characteristics of the Dines anemometer and the effect of adopting 3 s moving average gust, the wind gusts \hat{u} recorded during the period 1969–1981 were corrected according to [22]. We estimated the directional turbulence intensities (I_u) using the gust factor model proposed in [23] as follows:

$$GF = \frac{\hat{u}}{\bar{U}} \tag{1}$$

$$I_u = \frac{GF - 1}{0.42 \ln(3600/t)} \tag{2}$$

and then

$$z_0 = ze^{-1/I_u} \tag{3}$$

where, GF , z , t are the gust factor, measurement height above the ground and gust duration ($t = 3$ s), respectively.

The friction velocity u_* was calculated using the logarithmic-law velocity profile

$$U(z) = \frac{u_*}{k} \ln\left(\frac{z}{z_0}\right) \tag{4}$$

and then the corresponding gradient wind speed U_g was estimated with the relationship given by:

$$U_g = \frac{u_*}{k} \left[\ln\left(\frac{u_*}{fz_0}\right) + 1 \right] \tag{5}$$

where k and f are the von Kármán constant (0.41) and the Coriolis parameter, respectively. Then, the gradient wind speed was used to convert u_* to its equivalent value in the standard conditions. The logarithmic law velocity profile was used with the calculated standard u_* to evaluate the standard \bar{U} . The standard \bar{U} was then multiplied by the gust factor calculated by using the Cook model [23] to determine the standard \hat{u} . Finally, the directional \hat{u} correction factors were calculated by dividing the standard \hat{u} by the measured \hat{u} . The directional \hat{u} correction factors estimated for each of the two stations were then applied to the observed maximum gust speeds to convert the recorded gusts to the equivalent values in the standard conditions.

2.3.2. Extreme Value Analysis Applied to the Homogenised Data

The peaks over threshold (POT) method was subsequently applied to identify independent extreme gust events from the homogenised time series, covering the periods 1 January 1973–31 December 1981 and 21 October 1991–31 December 2020. The optimal threshold value for the application of the POT method, i.e., 27.4 m/s, was selected according to the parameter stability plot and mean residual life plot [3]. A declustering time window of 72 h was applied. The generalised Pareto distribution (GPD) was then used to model the excesses above the threshold, while the exceedances were assumed to occur according to a Poisson distribution.

For each of the two periods mentioned above, missing data gaps shorter or equal to 3 h were filled by linear interpolation and gaps longer than 3 h by means of the gust data extracted from the ERA5 climate reanalysis at the grid point closest to the St Mary’s Airport weather station. The ERA5 data were obtained through the Copernicus Climate Change Service (<http://climate.copernicus.eu/>, accessed on 24 January 2021) implemented by the European Centre for Medium-Range Weather Forecasts (ECMWF).

2.4. Extreme Wind Load Calculation

To approximate the extreme wind loading on the helideck, this work solves the incompressible Reynolds-averaged Navier-Stokes equations using OpenFOAM’s (version 4.1, <https://openfoam.org/>, accessed on 10 July 2022, The OpenFOAM Foundation Ltd, London W13 3DB, UK) pisoFoam solver and the $k-\omega$ SST turbulence closure model. This provides a high-fidelity solution for the fluid (air) flow around the structure, including viscous effects and high temporal and spatial resolutions for the aerodynamic loading due to the extreme wind conditions.

However, CFD simulation of extreme wind loading on such a complex structure is extremely challenging. If one considers the individual components of the structure in isolation, then according to

$$Re = \frac{\rho u L}{\mu} = \frac{\rho L}{\nu} \tag{6}$$

The Reynolds numbers for the frame elements (Re_{frame}), lantern housing ($Re_{lantern}$) and tower (Re_{tower}) are $1.83 \times 10^{+5}$, $7.99 \times 10^{+6}$ and $1.26 \times 10^{+6}$, respectively, (where, ρ is the density of fluid and is taken to be 1.225 kg/m³ based on the International Standard Atmosphere (ISA) values for dry air, at 15 °C, at sea level, u is the fluid flow speed ($v_b = 27.1\text{m/s}$, see Sections 2.3.1 and 3.1), L is the characteristic linear dimension and is taken to be the diameter of the frame elements (100 mm), the lantern chamber (4356 mm) and the lighthouse tower top (6860 mm), respectively. μ and ν are the dynamic and kinematic viscosity of the fluid, which for air at 15 °C were calculated $1.81 \times 10^{-5} \text{kgm}^{-1}\text{s}^{-1}$

and $1.48 \times 10^{-5} \text{ m}^2\text{s}^{-1}$, respectively. Consequently, the flow regime around the helideck frame elements consists of a fully turbulent vortex street downstream and the flow regime for both the lantern chamber and the tower top is a re-established turbulent vortex street with a turbulent boundary layer and a thinner wake downstream [24].

Therefore, due to the anticipated asymmetric flow regime (including vortex-shedding), the numerical model cannot take advantage of the geometric symmetry of the problem to reduce the size of the computational domain (and, therefore, the computational resources required to solve the problem).

Furthermore, a high-resolution computational mesh is required to simulate accurately the flow field around, and the forces on, the structure. For turbulence modelling (specifically wall functions) to be effective, the maximum near-wall cell size, Δs , (limited by the requirement of a corresponding y^+) should not be greater than one third of the boundary layer [25] and is calculated as follows:

$$\Delta s = \frac{y^+ \mu}{U_{fric} \rho} \quad (7)$$

where, ρ and Re are the density of the fluid and the corresponding Reynolds number of the flow respectively and $U_{fric} = \sqrt{\frac{\tau_{wall}}{\rho}}$, $\tau_{wall} = \frac{C_f \rho u^2}{2}$ and $C_f = \frac{0.026}{Re}$.

Here, a maximum value of 100 is selected for y^+ (representing the minimum feasible mesh resolution on the walls, and a requirement for near-wall turbulence, and boundary layer, 'modelling' (as opposed to wall 'resolving' methods, which would require $y^+ < 30$ and much fine near-wall mesh resolutions). Even considering this compromise, the near-wall cell size that should be used on the frame (Δs_{frame}), the lantern housing ($\Delta s_{lantern}$) and on the tower top (Δs_{tower}) are 0.001 m (1 mm), 0.0014 m (1.4 mm) and 0.0015 m (1.5 mm), respectively.

As a consequence, the required computational domain size, mesh resolution requirements and available computational resource mean full 3-dimensional simulation of the entire helideck structure is not practical. As a compromise, in this work, a two-dimensional slice (horizontally through the helideck frame and lantern housing) is modelled in order to predict the horizontal loads on the helideck frame elements. As a result, the structure (along with the computational domain) effectively extends to infinity in both vertical directions and any vertical loading on the structure (or vertical fluid motion) is not modelled. To simplify the model, further, only vertical elements of the frame and the lantern housing are included (any influence from the horizontal frame elements, landing deck, safety netting or lighthouse tower top are not captured).

In order to design the computational domain/mesh, provide a measure of uncertainty in the CFD solutions and offer some form of validation for the numerical model, simulations were first performed considering a single frame element, and the lantern housing, in isolation, i.e., without interactions between the other elements in the structure, in 27.1m/s steady, uniform wind. These cases are equivalent to simulations of cylinders in uniform flow, for which significant research, and physical data, exists, e.g. [24].

A series of different meshes were used, with resolutions specified in Table 1 (where dx and dy refer to the background mesh resolution in region 1 (indicated in Figure 5 by a 1 in a circle)). In all cases, the background mesh was refined, by 3 and 2 levels in regions 2 and 3, respectively, using the quadtree refinement strategy and 5 buffer layers (number of cells between refinement levels).

Figure 6 shows a snapshot of the velocity field from the simulations of the frame element (left) and lantern housing (right) using the highest resolution mesh in each case. As expected, for the frame element case ($Re_{frame} = 1.83 \times 10^5$) a fully turbulent vortex street is present downstream of the cylinder (Figure 6 left) and for the lantern housing ($Re_{frame} = 7.99 \times 10^6$) a fully turbulent vortex street is present as well, but with a turbulent boundary layer and a thinner wake (Figure 6 right).

Table 1. Parameters describing the mesh resolution, near-wall layers and timestep for each mesh used in simulations of cylinders in isolation (see Figure 5 for definition of parameters).

Element	Mesh	dx (m)	dy (m)	Δs (m)	No. Layers	Layer Expansion Ratio	Total Number of Cells	Δt
frame	1	0.080	0.086	0.001	4	2	5233	0.00018
frame	2	0.040	0.046	0.001	4	1.6	17,851	0.00011
frame	3	0.020	0.024	0.001	3	1.6	62,579	0.00005
frame	4	0.013	0.016	0.001	2	1.6	139,111	0.000333
lantern	0	0.159	0.171	0.0014	4	1.8	68,847	0.00025
lantern	1	0.080	0.085	0.0014	4	1.8	263,738	0.00018
lantern	2	0.040	0.043	0.0014	3	1.8	1,013,048	0.000125

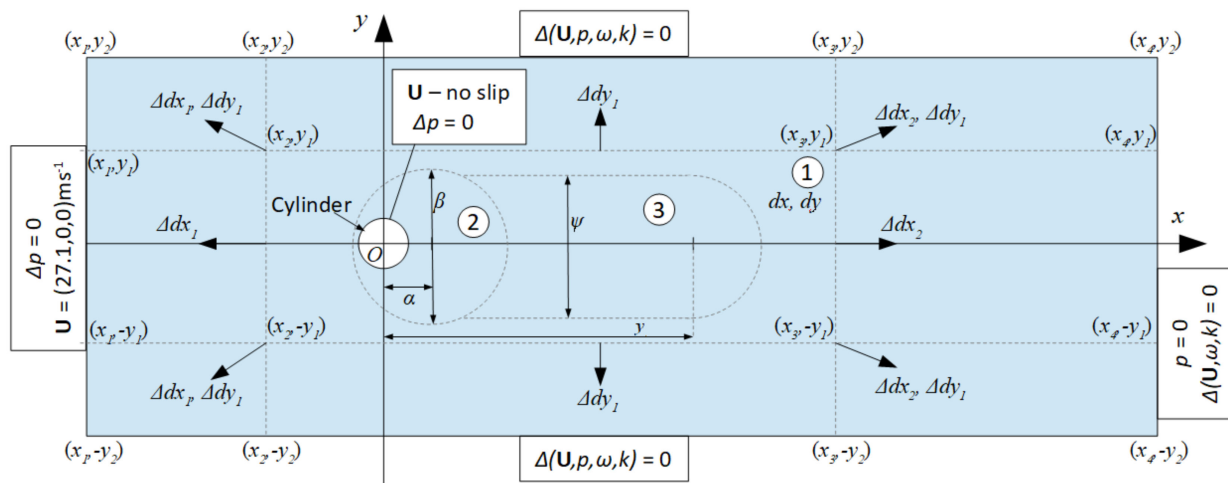


Figure 5. Schematic of the computational domain, mesh refinement regions and boundary conditions used in the isolated cylinder simulations.

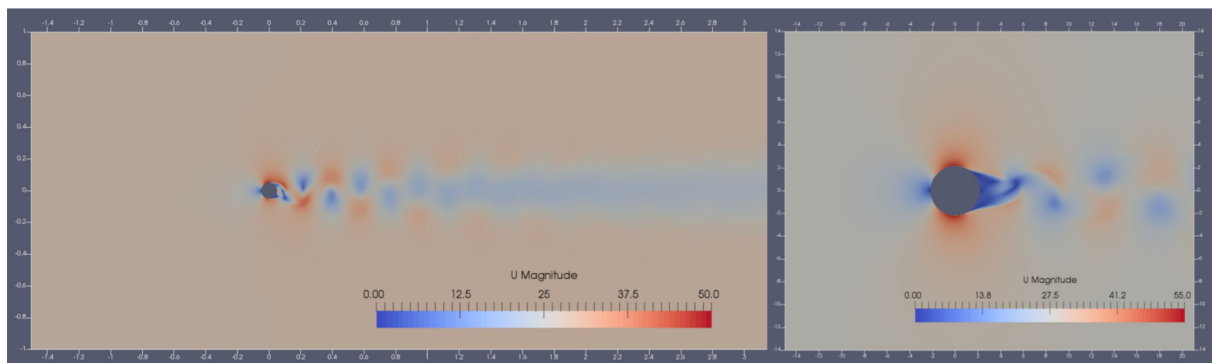


Figure 6. Flow speed around an element of the helideck frame (left) and the lantern in isolation (right).

However, for the frame element case, simulations using meshes 1 to 3 show noticeable differences in the amplitude (mesh 2, has significantly lower amplitude) and frequency of oscillations in load due to vortex shedding, but, in general, these three meshes predict fairly consistent mean drag coefficients of approximately 1.27. This is reasonably consistent with the prediction of $CD = 1.2$, from [24], but is greater than anticipated. The results for mesh 4 (the finest mesh) are considerably different and predict a significantly lower drag coefficient of approximately 1.05. These results demonstrate unfavourable ‘convergence’ behaviour and, as a result, for the prediction of drag coefficient, in these simulations the discretisation uncertainty alone is at least 10%. This level of uncertainty might be anticipated, and is also present in the empirical data [24] when simulating conditions in the turbulence transition region.

For the lantern housing, the drag coefficients in the ‘mesh convergence’ study showed a similar behaviour to that for the frame element, i.e., the solution does not converge and the discretisation uncertainty is high. Even though, the simulations showed a lower drag coefficient (between 0.3 and 0.5), which is lower than experimental data (0.71) reported in [24], the results are plausible due to the very large scatter, and rapidly varying relationship between CD and Re, in results reported at these Reynold’s numbers. This is due to the sensitivity of the system, at these high Reynolds numbers, due to the transition to a turbulent boundary layer and the upstream turbulence, which is evident in the empirical data presented in [24].

The simulation of the flow around the helideck frames and lantern was run on a desktop computer with an Intel Core i7-5820k CPU @ 3.30GHz (12-threads) and 32 GB of RAM (www.intel.co.uk, accessed on 13 July 2022, Swindon, UK). The simulation used 8 threads and took 170 h for 10s of simulated time.

2.5. Modal Testing

We used a set of six version 1 (V1) APDM Opal AHRS (attitude and heading reference system) devices. One Opal comprises a triaxial accelerometer, a triaxial rate gyroscope and a magnetometer. It records acceleration and rotation vectors in the local coordinate system (LCS, Figure 7A) of the Opal at each time stamp and computes orientation information in the form of quaternion vector at each time stamp. The quaternion derives from the combination of sensor signals and can be used in post-processing to recover world coordinate system (WCS) vectors for gyroscope and acceleration signals. WCS is referenced as a North, West and Up (NWY) triad. We attached 53 accelerometers on the helideck structure as shown in Figure 7B,C. The accelerometers on the helipad (shown in yellow in Figure 7C) were aligned with their LCS in common and rotated 90 degrees clockwise (viewed from above) with respect to NWU (i.e., WCS) and on the helideck posts (shown in red and green in Figure 7C), LCS was always aligned with Z direction facing inboard. Measurements were made in a sequence of seven swipes, moving four Opals and keeping two fixed. For each swipe, about one third of the duration was ambient response to light wind and machinery, one third with random walking around the helideck and one third hitting one of the vertical posts with a rubber mallet (as shown in Figure 7D).

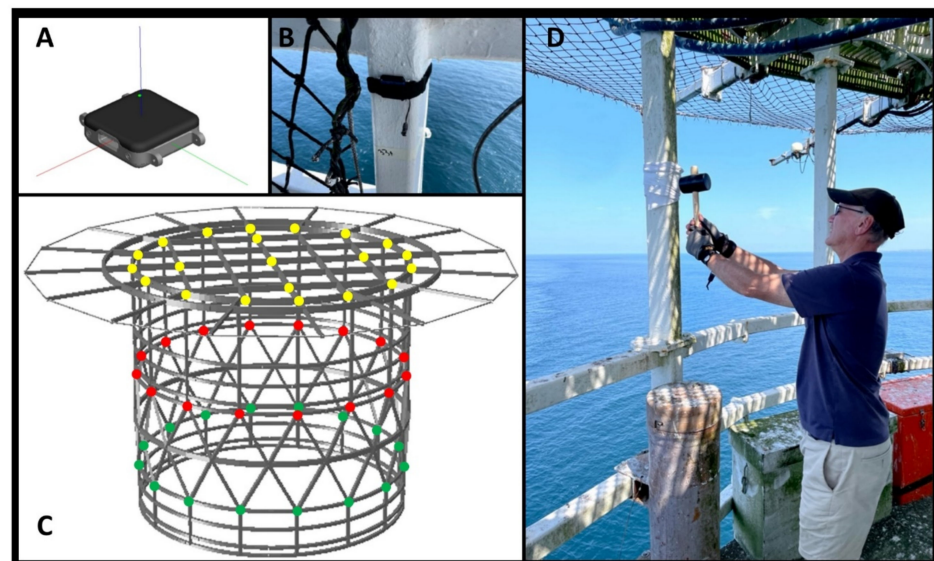


Figure 7. (A): APDM Opal IMUs; a triaxial accelerometers with $128 \mu\text{g}/\sqrt{\text{Hz}}$ noise floor. (B): An accelerometer attached to the helideck. (C): The location of accelerometers installed on the helipad (Different colours represent different elevations on the structures. Yellow, red and green represent Top (helipad), middle and lower levels, respectively). (D): Inducing excitation on the helideck to record the acceleration.

2.6. Design Computational Framework

The helideck structure consists of a landing platform and a supporting structure which is anchored to the masonry lighthouse lantern gallery by embedded holding down bolts. The structure is a cylindrical beam structure featuring horizontal, vertical and diagonal members (as shown in Figure 2B for the current structure, and Figure 8A for one of the helideck structures considered in this work). Our design space is limited to beam structure due to manufacturing and installation considerations. Here, we generate a design space which includes different configurations of network of connected beams.

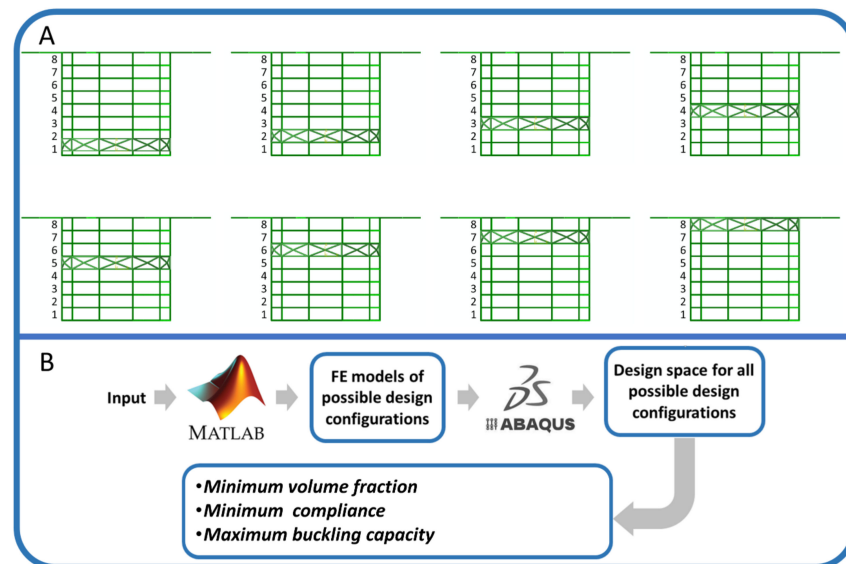


Figure 8. (A): Different locations of a helideck structure with 8 sections and 1 section of diagonal bracing. Different location of diagonal beams results in different compliances and buckling capacities. (B): The flowchart of the design space generation.

2.6.1. Material

The current helidecks are made of carbon steel which increases the risk of corrosion as shown in Figure 4 in the harsh environmental condition of lighthouses. We chose Aluminium 6082 T6 with filler material grade 403 for the next generation of helidecks for lighthouses as it is light and durable in such an environmental condition. The material selection was based on discussions with the partners of the project, namely, Aluminium Federation (ALFED) and material suppliers and manufacturers. The selected material has yield stress of 260 and 125 MPa according to Eurocode 9 for extruded and welded sections respectively [26]. In this work we chose the yield stress recommended by the code for welded section as the allowable stress.

In this work we modelled both the current structure (made of carbon steel) and the new designs in the design space (made of aluminium) in ABAQUS. The material properties we used in the FE simulations are presented in Table 2 and are adopted from [26,27]. We used 3-dimensional beam elements (element type B31 in ABAQUS) to model the helideck structure and discretised each component of the structure (i.e., free span of beams between any two connection points) by at least 5.

Table 2. Material properties used for the FE simulations.

Material	Type of Analysis	Constitutive Material Model	Elastic Modulus (E)	Poisson's Ratio (ν)	Yield Stress (σ_{yield})
Steel	Modal	Elastic	200 GPa	0.3	—
Aluminium	Static	Elastic	70 GPa	0.3	—
Aluminium	Riks	Elastic-Perfect plastic	70 GPa	0.3	125 MPa
Aluminium	Explicit	Elastic	70 GPa	0.3	—

2.6.2. Exploring Different Topologies for the Lightest Helideck

We have developed a computational framework to generate different topologies of a cylindrical beam structure for the helipad structure. We have developed a code in MATLAB (uk.mathworks.com, accessed on 10 July 2022, UK) which generates FE models of different topologies, runs the FE simulations in ABAQUS and generates a dataset featuring the volume fraction and compliance of the structures and the maximum stress throughout each structure configuration. We then used this dataset to choose the topology which results in the minimum volume fraction and compliance while keeping the stress below the allowable stress [28–33]. The schematic workflow of this process is shown in Figure 8B. The MATLAB code gets the following items as the input and automatically generates the FE model of the helideck in ABAQUS:

- Helideck geometry:
 - Height of the helideck;
 - Diameter of the supporting structure;
 - Diameter of the landing deck;
 - Overall diameter of the helipad including the safety net beams;
 - Number of circumferential sections;
 - Number of vertical sections.
- The helicopter properties:
 - Total mass of the helicopter for which the helideck is designed;
 - Length of the skids of the helicopter;
 - Spacing between the helicopter skids.
- Wind load;
- Beams cross section.

After running the simulation for the entire design space, the MATLAB code reads the result of the simulations and sorts the design space based on their volume fraction and compliance. Then it selects the lightest structure with the minimum compliance. The principals of topology optimisation for minimising the compliance are as follows:

$$\text{minimise } \Phi(u) = F^T u$$

$$\text{Subject to } \int \rho dV - \bar{V} \leq 0$$

where the objective function Φ is the static compliance, which is a function of the load vector F and the displacement vector u . ρ and dV are the density and volume of each element of the structure, and \bar{V} is the volume constraint [34]. In this work, we aimed at reducing the total mass of the structure by 50% in the topology optimisation process therefore we assumed $\bar{V} = 0.5$.

Here, we considered the structures with 16, 14, 12, 10 and 8 circumferential sections and 8 vertical sections. Diagonal bracing has been considered to be between one to eight layers (latter is considered as the fully braced structure) and any possible location of bracing has been considered. One hundred and eighty possible configurations have been considered and corresponding FE simulation was carried out to generate the design space.

The volume fraction of each structure was calculated by dividing its mass by the mass of the heaviest structure in the design space which is the one with 8 and 16 vertical and circumferential sections respectively and is fully braced by diagonal beams. The minimum and maximum values of volume fraction of the structures in our design space are 44% and 100 %, respectively, as shown in Figure 9.

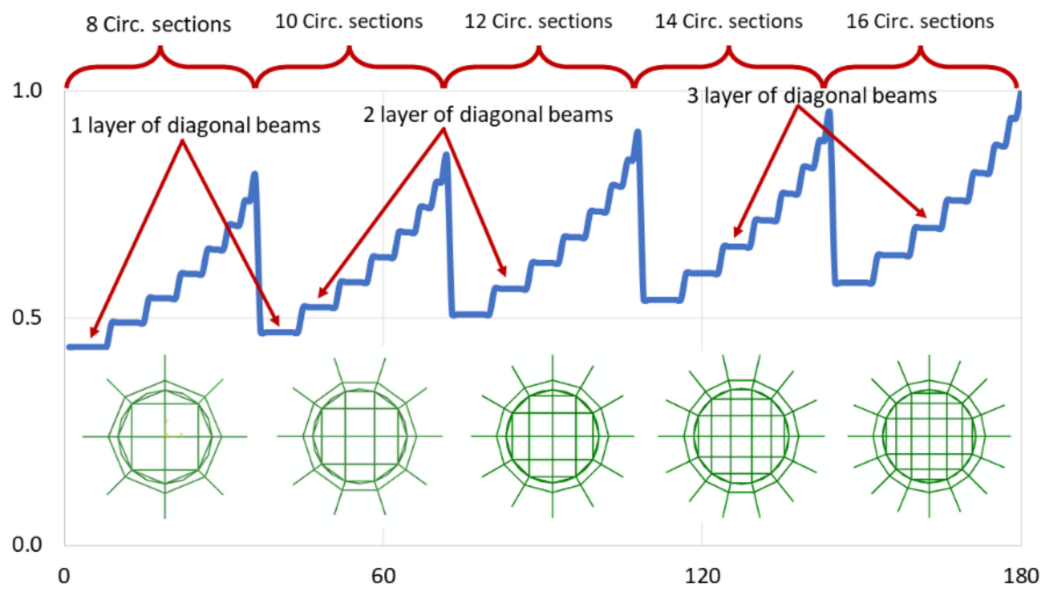


Figure 9. Volume fraction of all structures in the design space. The plan view of the helideck structures is shown below the volume fraction curve.

2.6.3. Loads

The helideck should be designed to withstand the loads which are likely to be applied on the structure when the helicopter lands. We adopted the loads recommended by “Standards for offshore helicopter landing areas—CAP 437” [35]. The following loads were simultaneously applied on the helipad structure and are schematically shown in Figure 10:

- Dynamic load due to impact landing

It is recommended by CAP 437 that the total mass of the helicopter to be applied by a safety factor of 2.5 to consider the dynamic effect of an emergency landing event. According to CAP 437, the supporting structure shall maintain the landing load regardless of the landing position on the helipad, therefore we considered the worst case, i.e., edge landing, which produces the highest bending moment throughout the structure.

- Sympathetic response of landing platform

It is recommended to increase the abovementioned dynamic load to include the effect of structural response depending upon the natural frequency of the helideck structure. A 30% increase is recommended by CAP 437.

- Overall superimposed load on the landing platform

A 0.5 kN/m² load should be applied on the helipad to consider the presence of any appendages on the deck surface in addition to the landing load.

- Lateral load on landing platform supports

The helideck structure should resist a horizontal load applied at the location of vertical landing load equal to 50% of the total helicopter mass. The direction of this load should be in a way that produces the worst loading condition.

- Dead load of structural members

This is the normal gravity load.

- Wind loading

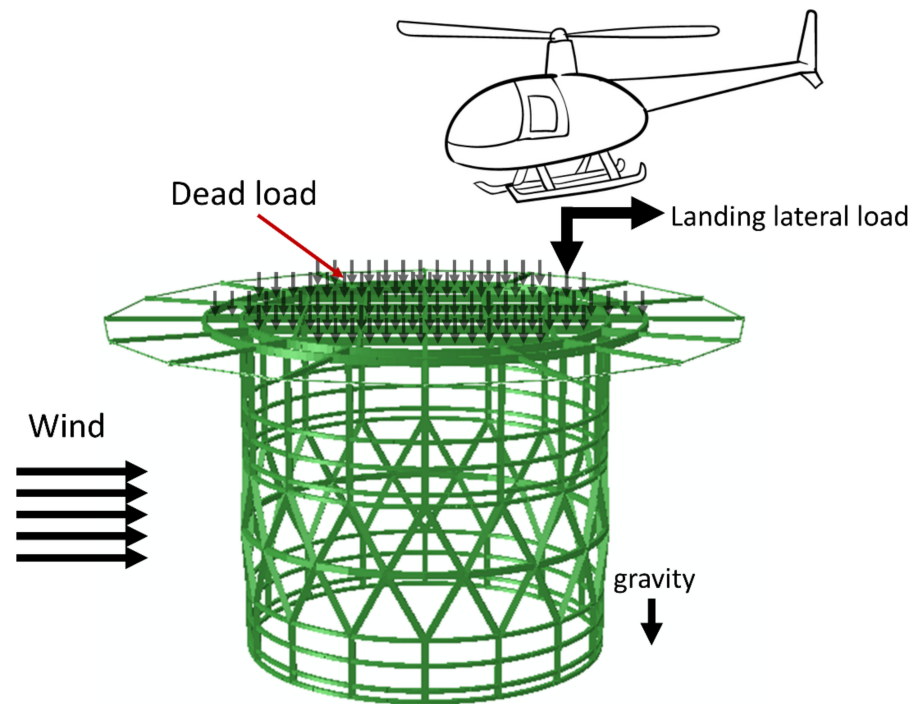


Figure 10. Applied loads shown on the current helideck structure on Bishop Rock lighthouse according to CAP 437 for edge landing scenario (all vertical posts at the bottom of the structure are anchored to the top of the lighthouse). According to the standard, the wind load and landing lateral loads are considered in the same direction to produce the worst case.

We calculated the actual wind load at the location of Bishop Rock lighthouse as described in Sections 2.3 and 2.4.

Using the abovementioned parameters, the MATLAB code generates FE model of each possible configuration of beam structures and load it based on the recommendations of the CAP 437.

After running this process and selecting the optimum structure with the minimum compliance (see Figure 11), we carried out further analysis namely post-buckling (i.e., Riks method) and wind dynamic (explicit) analyses, which are described in the following sections.

2.6.4. Buckling Analysis

We carried out non-linear buckling analysis of the structure which was selected by the algorithm described in Sections 2.2 and 2.3 by means of the Arc-length (Riks) method [36], which has been known as reliable method to calculate the buckling behaviour of Aluminium alloys [37]. This method is an incremental approach in which the defined loads on the structure are increased in every increment to get to the collapse point [7,38]:

$$P_{total} = P_0 + \lambda(P_{ref} + P_0) \tag{8}$$

where, P_0 is the dead load, P_{ref} is the reference load vector which is indicating the applied load on the structure and λ is the load proportionality factor. We used the ABAQUS software package to carry out the Riks analysis and calculate the maximum load proportionality factor of the structures. We assumed P_0 equal to zero so the load proportionality factor would be the ratio of the applied load on the structure at each increment over the reference loads defined in Section 2.6.3:

$$\lambda = \frac{P_{total}}{P_{ref}} \tag{9}$$

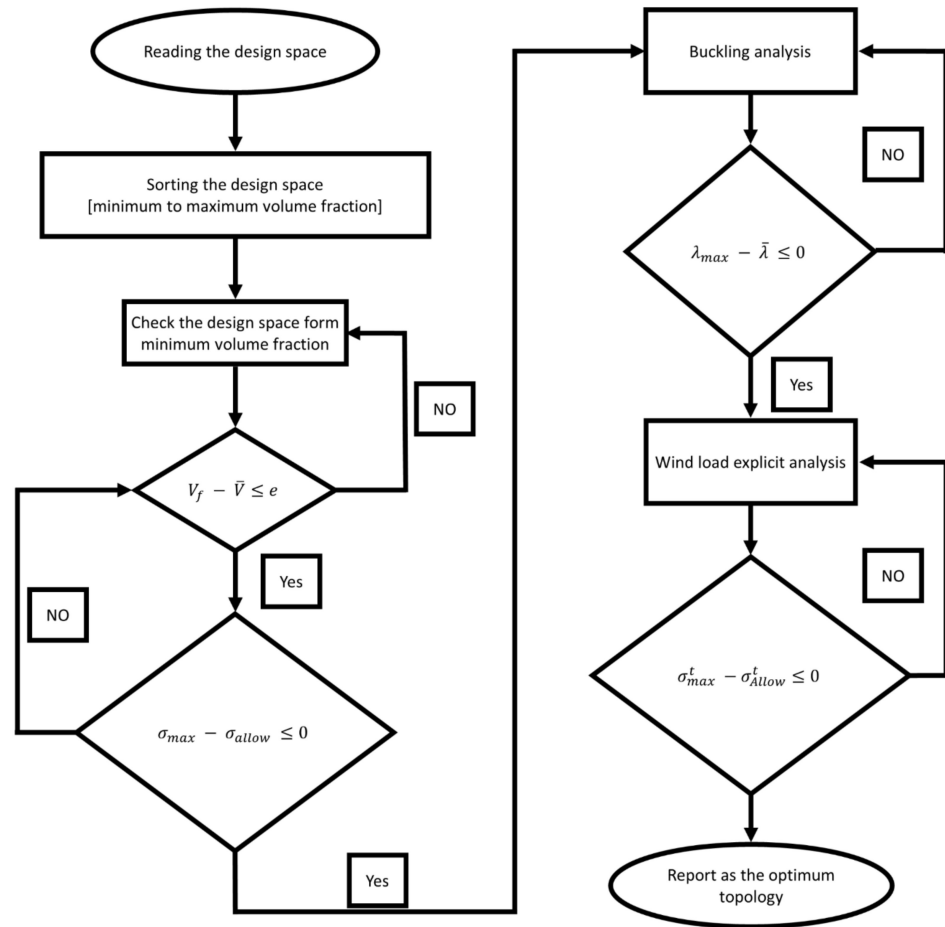


Figure 11. The workflow of selecting the lightest structure in the dataset with the minimum compliance.

Then we used λ as an indicator to compare the maximum buckling capacity of different designs.

2.6.5. Dynamic Analysis of the Wind Loading

We carried out explicit finite element analysis of the structure under varying wind load for a time period of 10 min as recommended by the CAP 437. We calculated the wind fluctuation for the average value of 27.1 m/s (see Sections 2.3 and 3.1) according to [39,40] as shown in Figure 12.

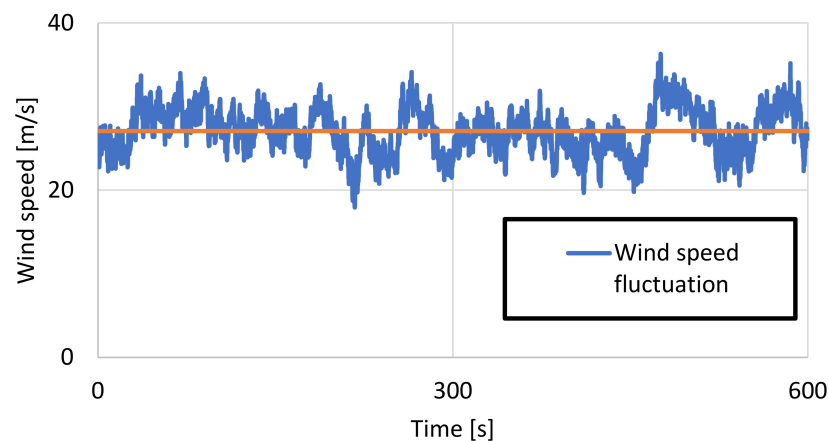


Figure 12. The wind fluctuation calculated for the location of the Bishop Rock lighthouse over a period of 10 min (600 s).

Using the wind fluctuation and the equations presented in Section 2.4, we calculated the wind load as a function of time and location on the helideck structure. We used these time-dependent forces with other loads presented in Section 2.6.3 to carry out explicit FE analysis for the assessment of the helideck over a period of 10 min according to the CAP 437.

3. Results

3.1. Extreme Value Estimates of Gust Speed

The return level plot for the GPD model based on the selected threshold value of 27.4 m/s is shown in Figure 13. From this plot a return level of 37.8 m/s is obtained at St Mary’s for a return period (T_R) of 50 years and a return level of 39.1 m/s is estimated for a return period of 100 years. Asymmetric 95% confidence intervals for each return level have been calculated through the profile log-likelihood method. The extreme value estimates are shown in Table 3 where the corresponding 10 min mean wind velocity is also reported. The gust factor model proposed by Cook [22] was used to convert the 3 s gust speeds to the hourly mean values and subsequently a factor of 1.06, as indicated in [25], was applied to convert the hourly mean values to the 10 min mean wind velocities.

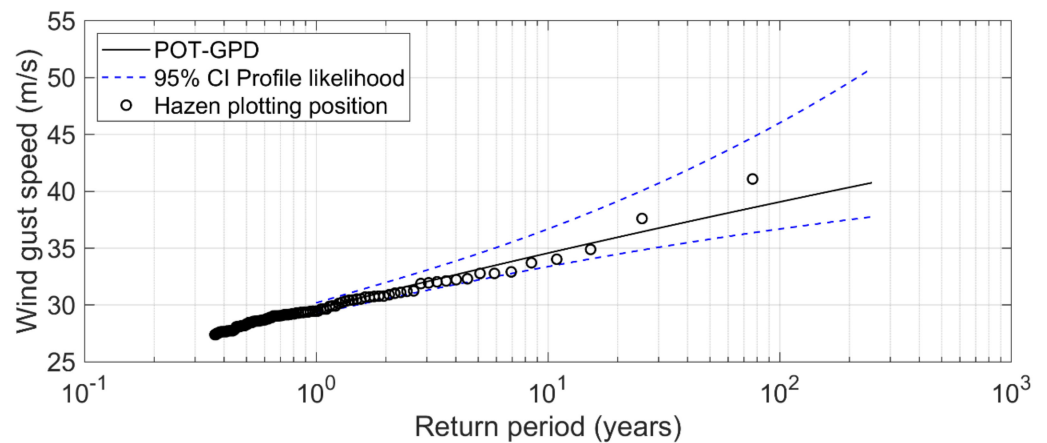


Figure 13. Return level plot for the GPD model fitted to the maximum gust speed at St Mary’s, based on the selected threshold of 27.4 m/s and declustering time window of 72 h. The associated 95% confidence interval is also shown with dashed blue lines.

Table 3. Estimates of 3 s gust speed for different return periods (T_R , years) and corresponding 10 min mean wind velocity at St Mary’s.

T_R (Years)	3 s Gust Speed (m/s)	10 min Mean Wind Velocity (m/s)
2	31.2 [30.6;32.0]	21.6 [21.2;22.2]
10	34.6 [33.4;36.7]	23.9 [23.1;25.4]
20	36.0 [34.5;39.1]	24.9 [23.9;27.1]
50	37.8 [35.8;42.8]	26.2 [24.8;29.7]
100	39.1 [36.7;46.0]	27.1 [25.4;31.9]
150	39.8 [37.2;48.1]	27.6 [25.8;33.3]
200	40.3 [37.5;49.6]	28.0 [26.0;34.3]
250	40.8 [37.8;50.8]	28.2 [26.2;35.2]

Considering an extreme event with a 0.01 annual exceedance probability (corresponding to an event with a return period $T_R = 100$ years) and following the EN 1991 1 4: 2005 + A1: 2010 and the UK National Annex (BSI, 2011a,b) we used the basic wind velocity $v_b = 27.1$ m/s in this work.

3.2. Wind Load on the Helideck as Function of Time and Location

Using the method described in Section 2.4, flow field around, and the load on, a helideck structure with ten circumferential sections was calculated for an incident wind speed of 27.1 m/s. Figure 14 shows a snapshot of the 2D simulation, including the lantern housing, the ten vertical frame elements and the magnitude of the fluid (air) velocity. It is clear that the interactions between the elements considerably alters the fluid flow field compared to the cases of elements in isolation (see Figure 6).

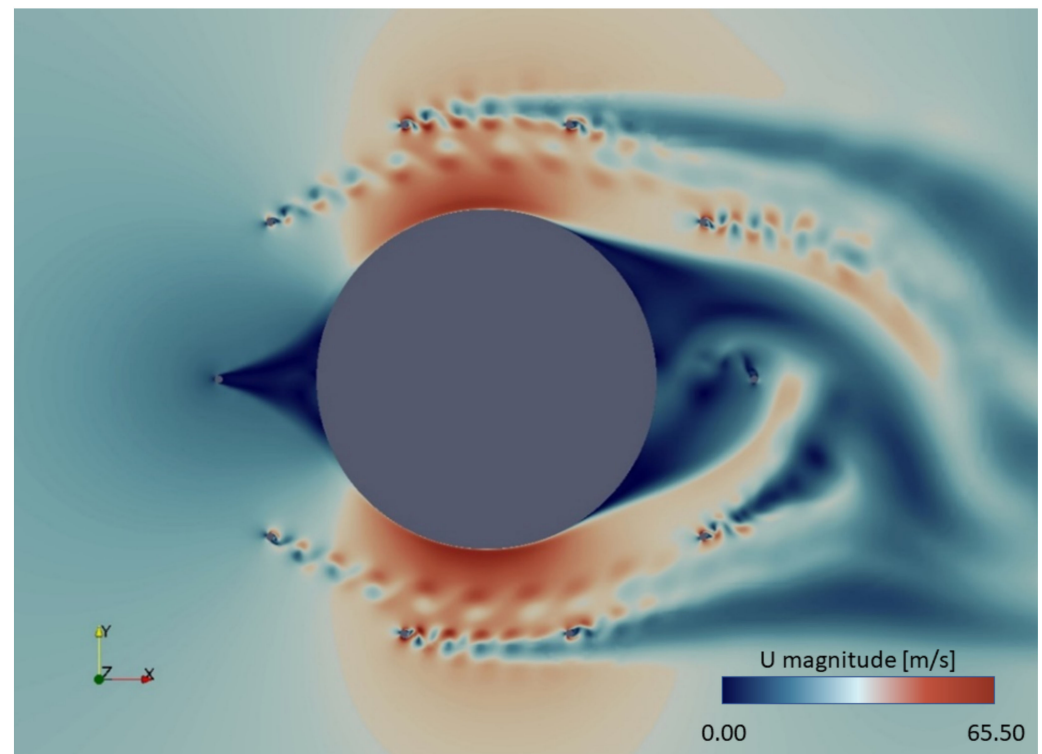


Figure 14. The velocity field in the vicinity of the vertical frame elements and lantern housing (Velocity, U , in m/s).

From this simulation, the mean values of drag and lift coefficient ($\overline{C_D}$ and $\overline{C_L}$, i.e., coefficient of force in streamwise and perpendicular direction, respectively) are calculated for all the frame elements of the helideck. Figure 15 shows that the interactions between the cylinders considerably alters the load experienced by any particular element and that the mean load depends strongly on the relative position of the element in the structure. It also shows that the mean drag coefficient can be significantly greater than that experienced by a frame element in isolation ($C_d \sim 1.2$), and non-zero mean lift coefficients are possible, due to the acceleration of air flow around the lantern housing.

In addition to the mean loads, the fluctuations in the loads experienced by the frame elements due to the vortices is also influenced by the interactions between the various elements. To find the amplitude and frequency of the load oscillations, a fast Fourier transform (FFT) has been performed on the time series of the coefficients for each of the frame elements. Figure 16 shows the amplitude spectra for the drag and lift coefficients. For each element the amplitude and frequency associated with the primary peak are depicted in Figure 17. It is shown that some of the signals have other significant peaks, e.g., for elements 3 and 9 there are peaks in the C_D spectrum between 0.06 and 0.08 and peaks for C_L spectrum between 0.24 and 0.16 at frequencies of approximately 56.2 Hz and 74 Hz, but in general, these other peaks are an order of magnitude lower in amplitude.

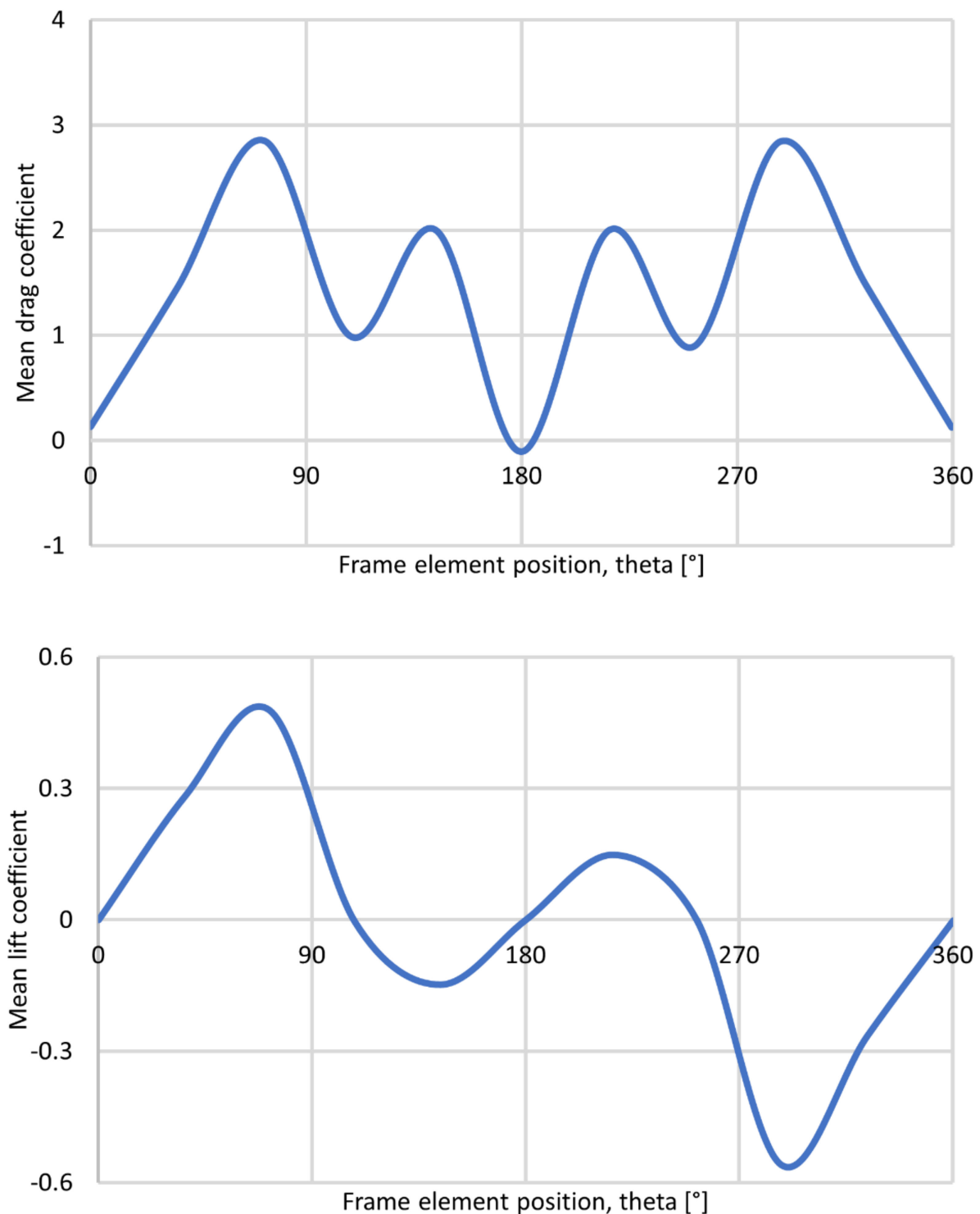


Figure 15. Mean drag (top) and lift (bottom) coefficient on the vertical helideck frame elements as a function of their angular position around the lantern chamber, for an incident wind speed of 27.1 m/s.

It is shown in Figures 15 and 17 that the elements experiencing the greatest mean drag also experience the greatest amplitude of oscillation in both drag and lift. Furthermore, for elements experiencing the greatest amplitude of oscillation, the frequency of the oscillation is consistent with the expected frequency of vortex shedding for the isolated frame element in 27.1 m/s flow speed equal to 54.2 Hz [24], higher mean thrust coefficients lead to higher frequency oscillations and vice versa.

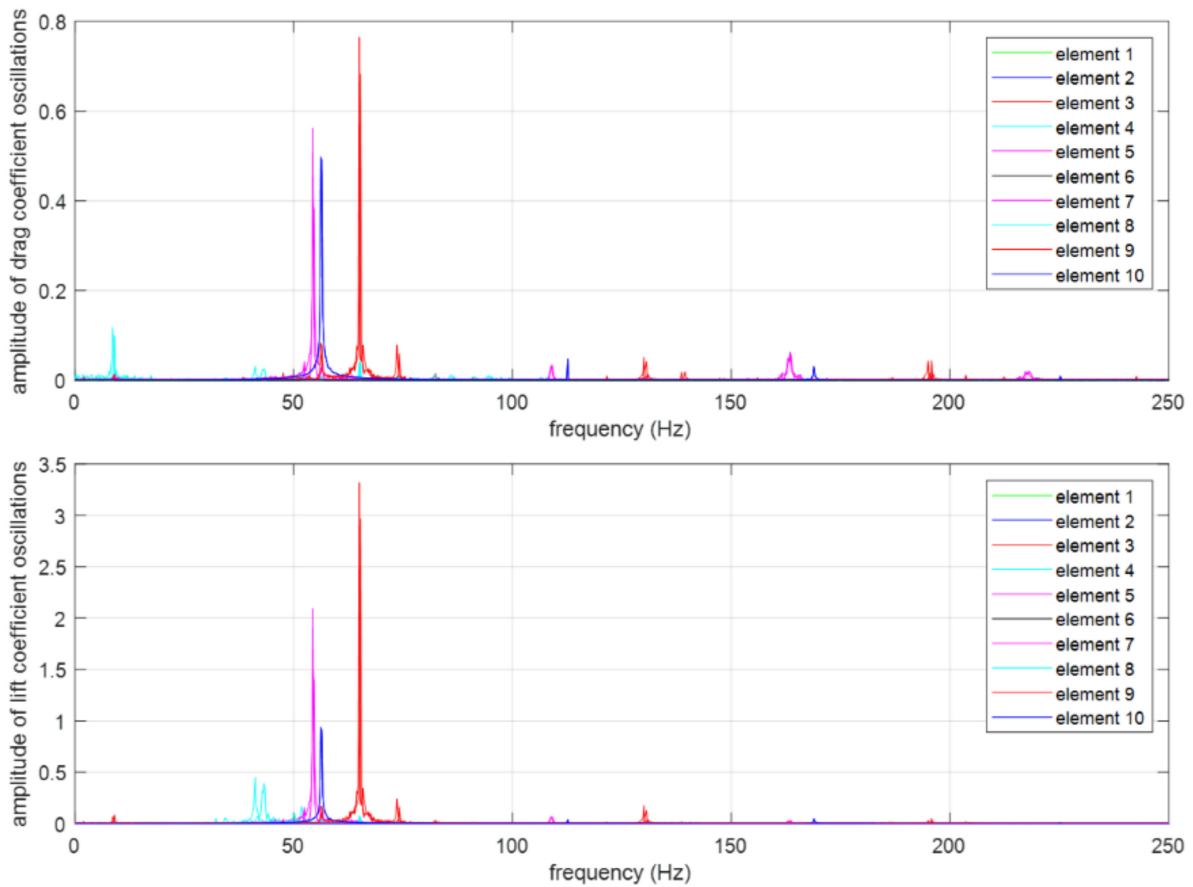


Figure 16. Amplitude spectrum (result of a FFT) for the oscillations in drag (**top**) and lift (**bottom**) coefficient for each of the helideck frame elements, for an incident wind speed of 27.1 m/s (the results for the frame elements have been colour coded based on the symmetry of their positions).

According to the result presented in this section, $F_{x,i}$ and $F_{y,i}$ which are the loads on the i th vertical element of the helideck frame in the stream direction and perpendicular to it respectively, can be approximated as follows:

$$F_{x,i} = \frac{1}{2} \rho A u^2 \left[\overline{C_{D,i}} + \alpha_{C_{D,i}} \cos \left(\frac{\varphi_{C_{D,i}} t}{2\pi} \right) \right] \tag{10}$$

$$F_{y,i} = \frac{1}{2} \rho A u^2 \left[\overline{C_{L,i}} + \alpha_{C_{L,i}} \cos \left(\frac{\varphi_{C_{L,i}} t}{2\pi} \right) \right] \tag{11}$$

where, $(\overline{C_{D,i}}$ and $\overline{C_{L,i}})$ are the mean drag and lift coefficients (Figure 15); $\alpha_{C_{D,i}}$ and $\alpha_{C_{L,i}}$ are the amplitudes of the primary oscillations in drag and lift coefficient respectively (Figure 17) and; $\varphi_{C_{D,i}}$ and $\varphi_{C_{L,i}}$ are the frequencies of the primary oscillations in drag and lift coefficient, respectively (Figure 17). ρ is the density of the air (1.225 kg/m³), A is the projected area the cylinder presents to the undisturbed flow, u is the wind speed in the streamwise direction (27.1 m/s), and t is time (in seconds).

Since the helideck is a circular structure, by linear interpolation of the result of the simulation for the case of a helideck with ten vertical frame element, we calculated the force as a function of θ and time where θ is the angle between the wind direction and the line that connects the location of interest and the centre of the helideck as shown in Figure 18. Therefore, we could estimate the wind force on the elements of helidecks with vertical frame elements less or more than 10. We applied mean value of the wind load for static and bucking analyses and the time-dependent wind force for the explicit dynamic analysis.

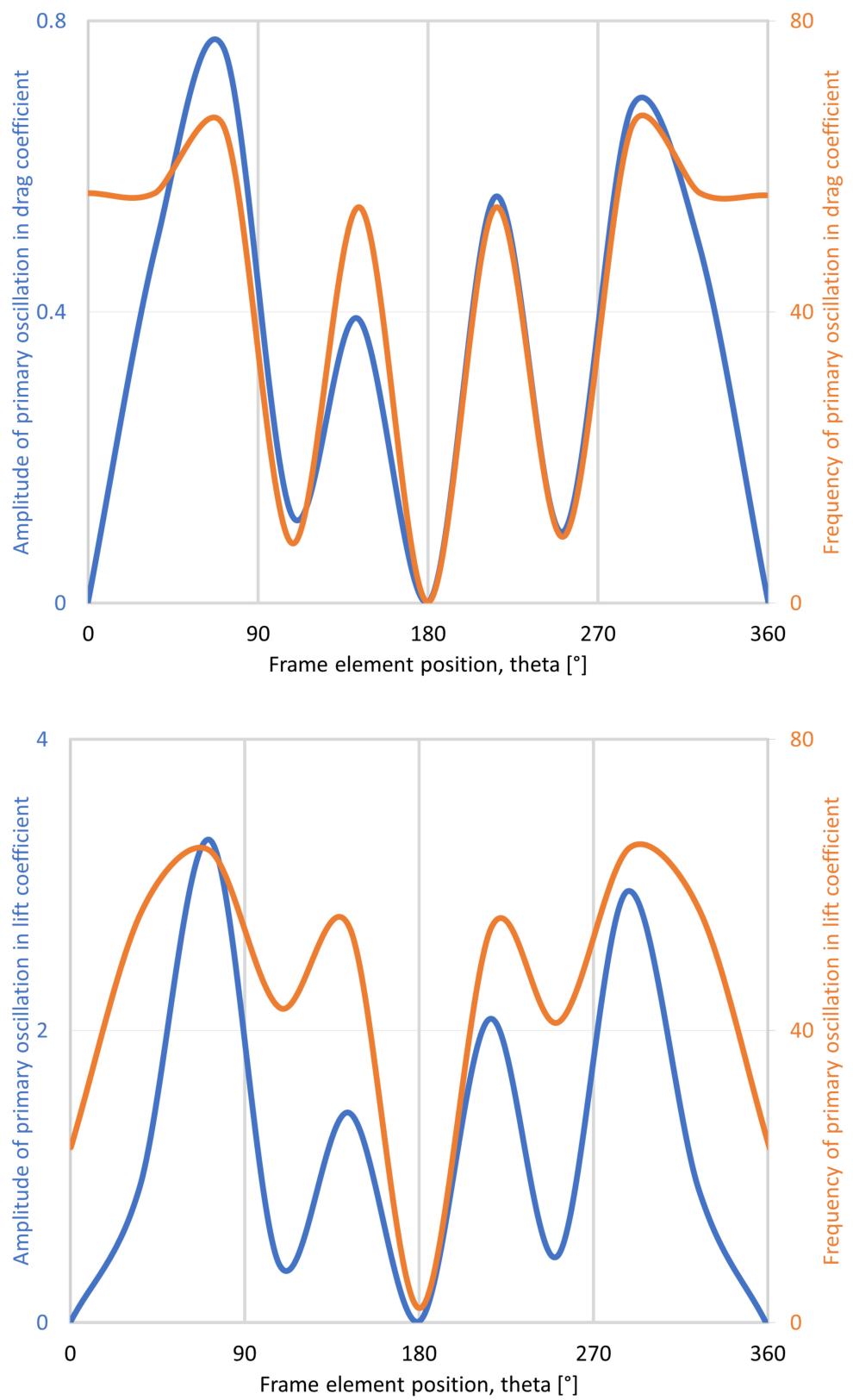


Figure 17. Amplitude and frequency of primary oscillation in drag (**top**) lift (**bottom**) coefficient for the helideck frame elements as a function of angular position for an incident wind speed of 27.1 m/s.

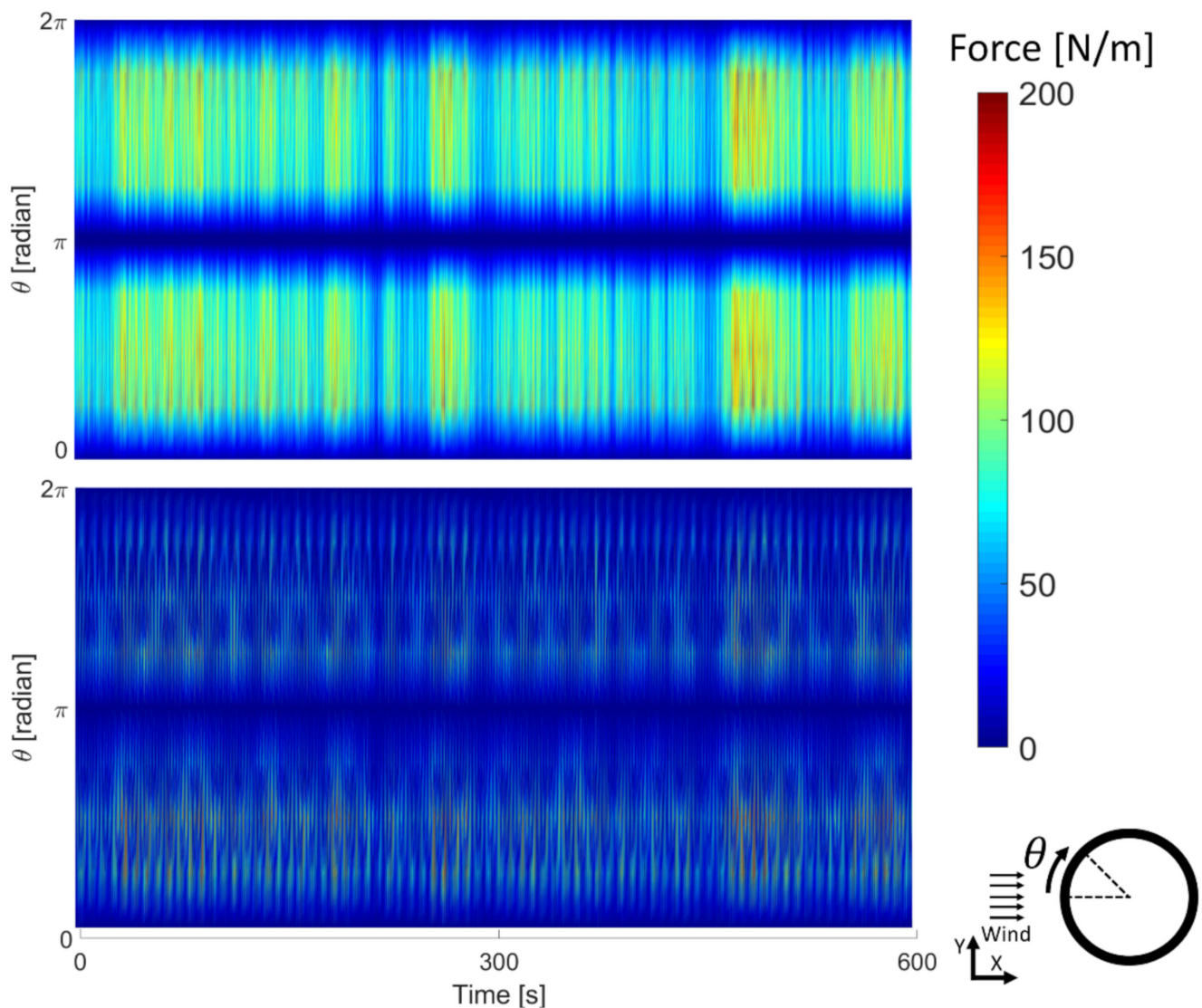


Figure 18. The wind forces per unit of length (Drag, (top), and Lift, (bottom), in x and y directions respectively) calculated for the Bishop Rock lighthouse helideck as function of location and time over a period of 10 min (600 s).

3.3. Modal Analysis

Figure 19 shows a sample time history of horizontal acceleration due to the mallet impacts. We used eigensystem realisation algorithm (ERA) to merge and normalise the cross-power matrices of the individual swipes with respect to some or all reference channels, and then we converted the merged cross-powers to cross-covariance (free decay) functions that are in effect curve-fitted in time domain [41].

The first three identified modes of vibration of the helideck are shown in Table 4. Moreover, we modelled the current helideck structure in ABAQUS and performed modal analysis to calculate its natural frequencies and compare the result of experimental evaluation with the numerical results. As shown in Table 4, the result of FE modal analysis of the helideck is in a good agreement with the experimental results with 6.2%, 5.1% and 6.9% of error for the first to the third mode of vibration, respectively.

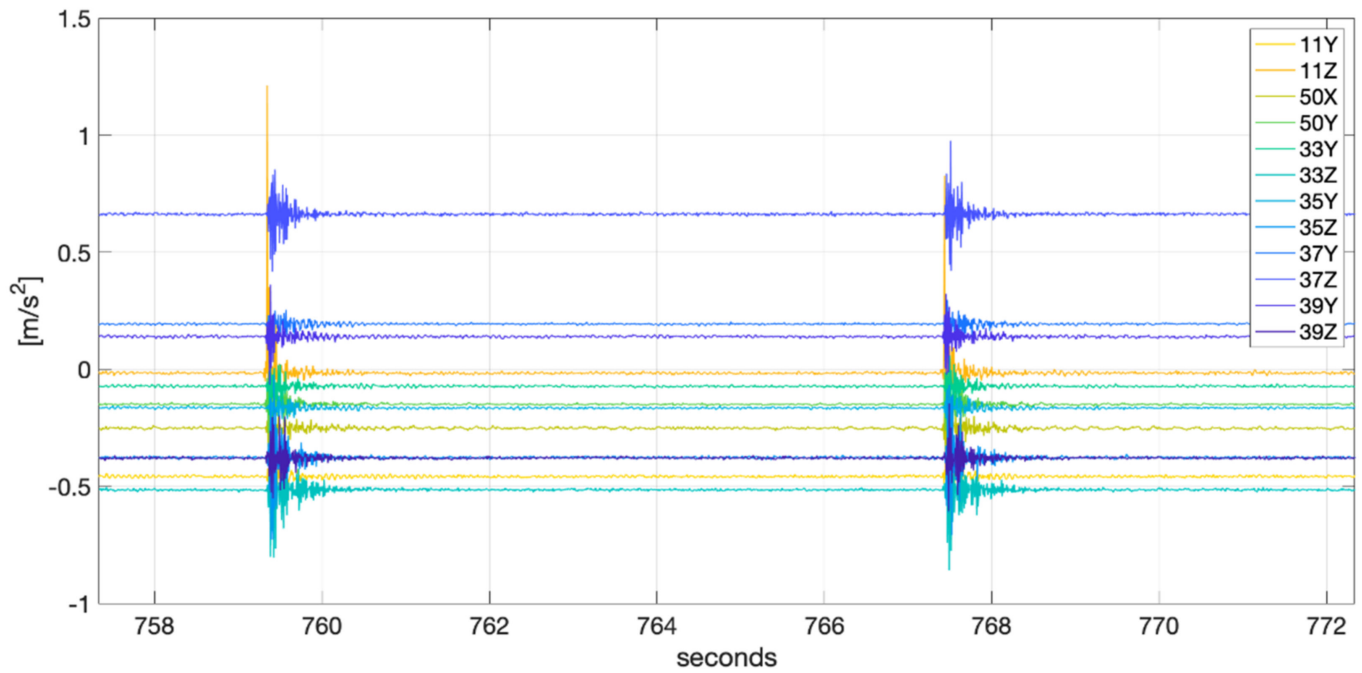


Figure 19. Acceleration time history for mallet impact excitation.

Table 4. Result of numerical and experimental modal analysis of the Bishop Rock lighthouse helideck for its first three vibration modes (the contours of showing the displacement magnitude where dark blue refers to zero and red indicates displacement equal or greater than 1 mm).

Mode 1		Mode 2		Mode 3	
Num.: 4.30 Hz	Exp.: 4.05 Hz	Num.: 4.30 Hz	Exp.: 4.09 Hz	Num.: 4.68 Hz	Exp.: 5.03 Hz

3.4. The Optimum Helideck Structure

We calculated the strain energy (which represents the compliance) of each structure in the generated dataset. Figure 20 shows the strain energy of the structures in the design space versus their volume fraction. According to the volume constraints ($\bar{V} = 0.5$), there are two groups of structures with volume fraction lower than \bar{V} , the ones with one and two layers of diagonal bracing with volume fractions of 44% and 46%, respectively. The minimum compliance for the structures with volume fractions less than 50% belongs to the structure with two layers of diagonal bracing with the bracing located in the lower part of the helideck. The maximum stress of all structures was measured and all structures in the design space had maximum stresses lower than the allowable stress varying between 25 to 64 MPa for the structures with the maximum and minimum compliance respectively. We

carried out buckling analysis of structures with one and two layers of diagonal bracing to find the best structure with the highest buckling capacity.

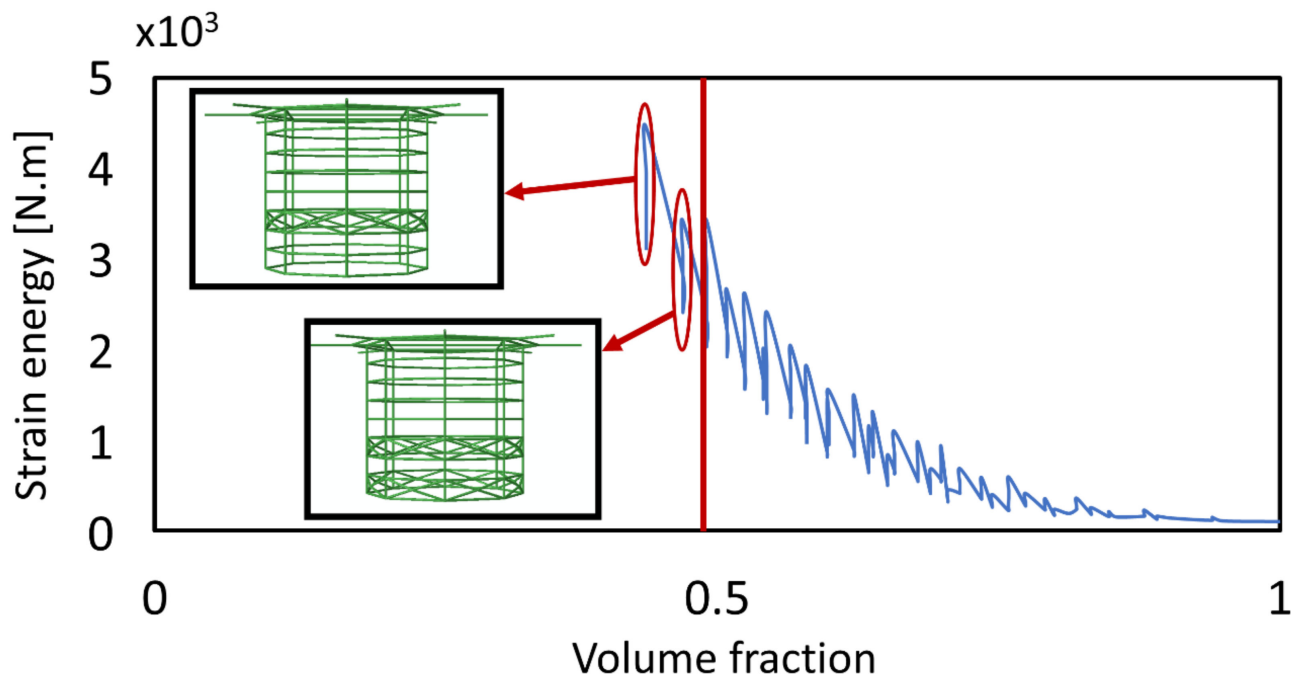


Figure 20. Volume fraction of the design space. Examples of the structures with the volume fraction lower than 0.5 are shown here.

3.4.1. Buckling Analysis

The results of the Riks analysis, which was carried for the structures with the volume fraction lower than 50% (structures with one and two layers of diagonal bracing), are shown in Figure 21. It is shown that they all would buckle above the reference loads described in Section 2.6.3. The load proportionality factor of these structures varies from 1.10 to 1.57 that means the helideck with one layer of diagonal bracing right under the helipad would buckle when the design loads are increased by 10% and the helideck with two layers of bracing one at the bottom of the helideck and the other one located at the third section from bottom of the helideck would buckle when the design loads are increased by 57%. We chose two structures out of two groups (i.e., structures with one and two layers of diagonal bracing) with the highest load proportionality factors in their groups (see Figure 21) for Dynamic (time-dependent) analysis.

3.4.2. Dynamic Analysis of the Wind Loading

The result of our explicit analysis shows that two structures respond to the time-dependent wind load similarly however the maximum stress over the time of simulation for the structure with only one layer of diagonal bracing is slightly higher than the one with two layers of bracing. Table 5 shows the result of static, Riks and dynamic analysis for the two structures featuring the volume fraction lower than 50% and have the highest buckling capacity. It is shown that the structure with two layers of diagonal bracing (shown in Table 5) has the highest buckling capacity and lower levels of maximum stress in both static and dynamic analyses.

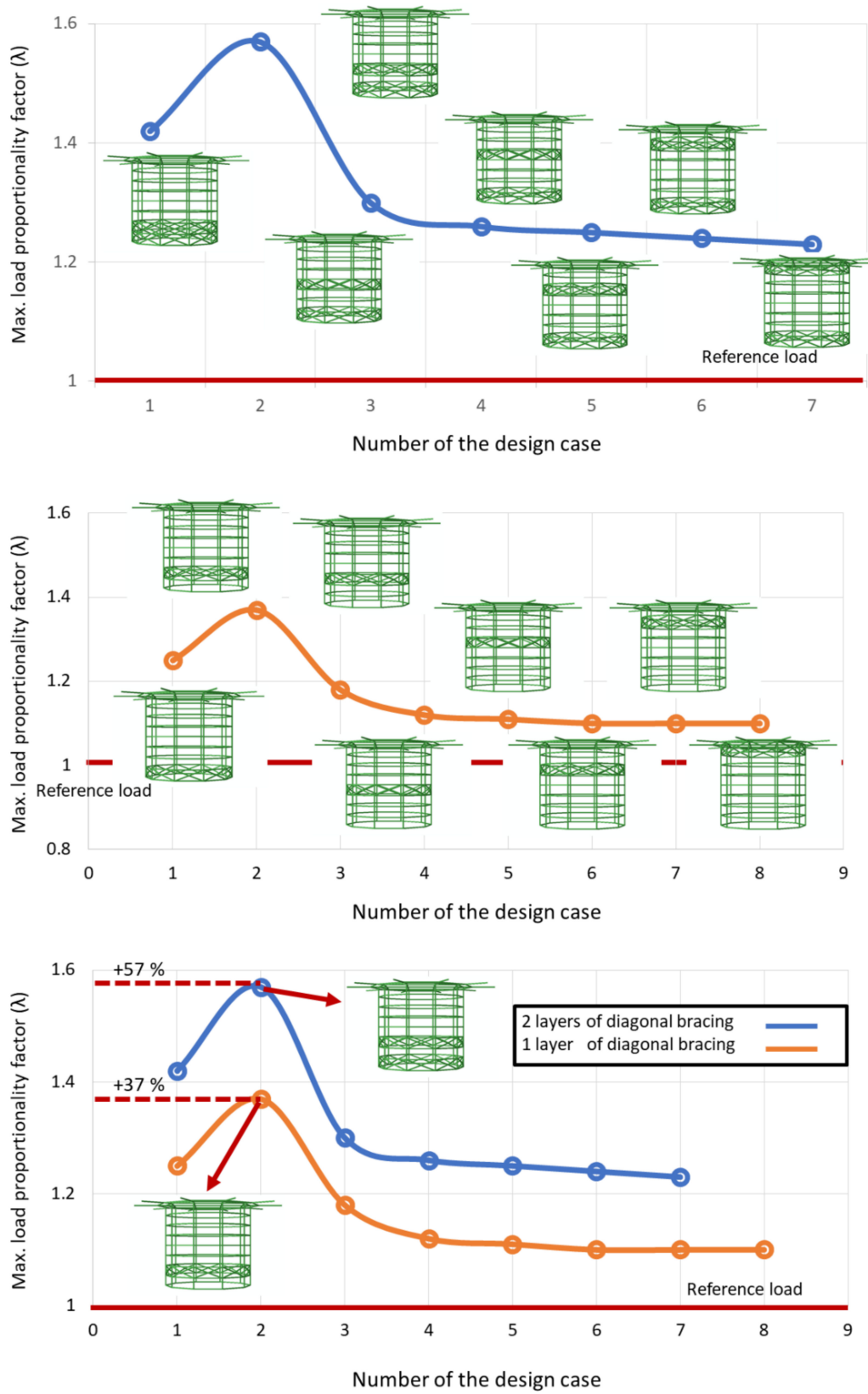
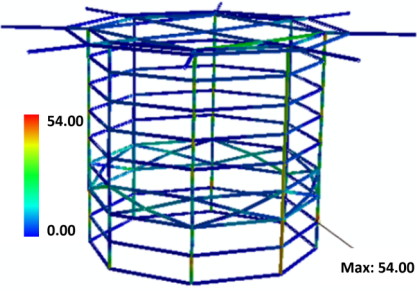
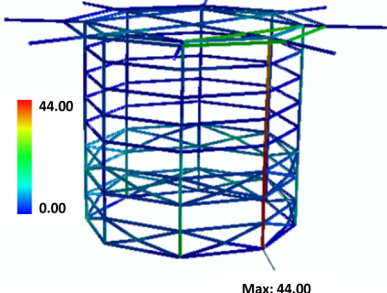
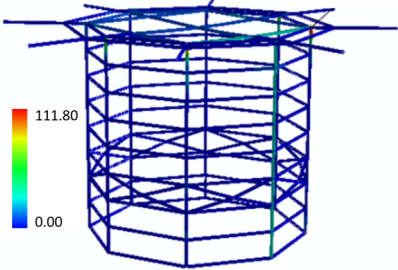
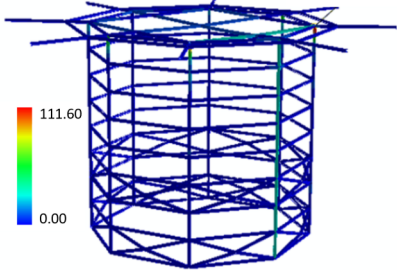


Figure 21. Maximum load proportionality factor for structures with one and two layers of diagonal bracing obtained from Riks analysis. **(Top):** the structures with two layers of diagonal components. **(Middle):** the structures with one layer of diagonal components. **(Bottom):** comparison of the load proportionality factor of the structures with one and two layers of diagonal bracing.

Table 5. Comparison of the results of static, Riks and dynamic analyses of the structures meeting all requirements.

Static Analysis		
Volume fraction	44%	46%
Maximum stress	54 MPa	44 MPa
Von_Mises stress distribution		
Riks Analysis		
λ	37%	47%
Dynamic (Time-Dependent) Analysis		
Average stress	56.3 MPa	55.8 MPa
Maximum stress	111.8 MPa (at 1790 s)	111.6 MPa (at 1440 s)
Von_Mises stress distribution		

4. Discussion

We have adopted a multidisciplinary approach to identify the environmental load on the Bishop Rock lighthouse helideck precisely and have developed a computational framework to find the lightest beam structure with minimum compliance for a helideck on this offshore lighthouses. Even though we focused on the Bishop Rock lighthouse in this work, the developed framework in this work can be used for other lighthouses and similar buildings.

A homogenisation procedure has been applied to the available gust speeds recorded at St Mary’s to remove discontinuities mainly due to changes in instrumentation, measurement height, observing practice and location. An extreme value analysis was performed applying the POT method to the homogenised data to determine 3 s gust speed estimates corresponding to return periods of 2, 10, 20, 50 and 100 years in the study area.

The effect of wind load on the helideck structure was estimated using CFD simulations. The result of our numerical model showed that the flow around the helideck structure due to the wind in extreme conditions is highly turbulent. We observed a rather high level of uncertainty due to the convergence of the model (more than 10%); however, such level of uncertainty was also observed in empirical study proposed by Cook [24]. Furthermore, we showed that the interactions between the cylinders considerably alters the fluid flow field (compared to the case of a cylinder in isolation). The mean thrust coefficient would greatly vary between the different helideck frame elements and, in some cases, was increased to more than double the value of an isolated element due to the acceleration of the wind around the lantern chamber. In addition, a variable, but considerable, mean lift

coefficient was observed due to these interactions, which would be assumed to be zero for an isolated cylinder.

Moreover, we carried out an experimental modal analysis for the current helideck structure which is in operation on the Bishop Rock lighthouse and described its modal behaviour. We also carried out computational modal analysis to estimate the natural frequency of this structure by means of finite element method. By comparing the result of our computational simulation and the experimental results of modal analysis, we observed average error of 6% between computational and experimental results for the first three modes of vibration of the helideck. The good agreement between the computational and empirical results showed that the type and size of elements and the constitutive material model we used in our FE model are properly representing the actual behaviour of the real helideck structure.

We developed a computational framework to generate a dataset for possible design configurations of the helideck structure. This work is the first attempt to optimise an offshore lighthouse helideck by considering the actual environmental loads for the location of the lighthouse. The computational framework showed that the structures with eight circumferential and vertical sections and with one and two rows of diagonal bracing are meeting the volume fraction constraint (50%) while maintaining their integrity under the static loads (maximum Von Mises stress observed throughout these structures was 64 MPa), regardless of the location of the diagonal bracing. Then we showed that the location of diagonal bracing rows influenced the buckling capacity of the structures (load proportionality factor λ) significantly. The Riks analyses showed that the structure with two rows of bracing has the maximum buckling capacity among the structures with the volume fraction lower than 50%, when there is one row of the diagonal bracing at the bottom of the structure and one at the third row of from the base of the helideck (see Table 5). Nevertheless, we found that in the case of transient wind load the structures with one and two rows of experiencing similar maximum stresses which could be due to local effect of stress concentration at the connection points [42–44] as shown in Table 5.

According to our multidisciplinary work, we found that the structure with eight vertical and circumferential sections featuring two rows of diagonal bracing with one at the base and the other one at the third section from the base of the helideck was the optimum design for the considered loading in this work. We followed a one-way coupled approach to reduce the computational cost [45]. We calculated the environmental loads by means of computational fluid analysis in this work and mapped the loads to the structure and we did not calculate the flow pressure field due to deformation of the structure. However, a fully coupled solid-fluid interaction results in a more accurate way, as proposed by E. Aursand et al., and K. Bergmeister [46,47], and may be addressed in future works. Here, we focused on the general configuration of the structure and chose a circular cross section with a constant thickness for the whole structure, nonetheless different cross sections with varying thicknesses may be addressed in future works as well.

Author Contributions: S.F.K. and D.D. designed the study; S.F.K., M.M., A.A., E.R. and J.M.W.B. performed the study; S.F.K. and M.M. acquired and analysed data; S.F.K., M.M., A.A., E.R. and J.M.W.B. wrote the paper; P.D. and D.D. reviewed the manuscript; and D.D. provided the team with funding. All authors have read and agreed to the published version of the manuscript.

Funding: Engineering and Physical Sciences Research Council (EPSRC) Impact Accelerator Award, grant numbers EP/V520342/1.

Institutional Review Board Statement: Not applicable.

Informed Consent Statement: Not applicable.

Acknowledgments: The authors gratefully acknowledge the UK Met Office, the British Atmospheric Data Centre and the Centre for Environmental Data Analysis for providing access to the MIDAS data. The authors would also like to acknowledge the support of Jan Lukaszewski [Aluminum Federation,

ALFED], Craig Barnshaw [ALUBEND] and Neil James [Righton Blackburns Bristol] for the material and profile selection process.

Conflicts of Interest: The authors have no conflict of interest.

References

- Raby, A.; Antonini, A.; D'Ayala, D.; Brownjohn, J.M.W. Environmental loading of heritage structures. *Philos. Trans. R. Soc. A* **2019**, *377*, 20190276. [[CrossRef](#)] [[PubMed](#)]
- Raby, A.C.; Antonini, A.; Pappas, A.; Dassanayake, D.T.; Brownjohn, J.M.W.; D'Ayala, D. Wolf Rock lighthouse: Past developments and future survivability under wave loading. *Philos. Trans. R. Soc. A* **2019**, *377*, 20190027. [[CrossRef](#)] [[PubMed](#)]
- Antonini, A.; Raby, A.; Brownjohn, J.M.W.; Pappas, A.; D'Ayala, D. Survivability assessment of fastnet lighthouse. *Coast. Eng.* **2019**, *150*, 18–38. [[CrossRef](#)]
- Brownjohn, J.M.W.; Raby, A.; Au, S.-K.; Zhu, Z.; Wang, X.; Antonini, A.; Pappas, A.; D'Ayala, D. Bayesian operational modal analysis of offshore rock lighthouses: Close modes, alignment, symmetry and uncertainty. *Mech. Syst. Signal Process.* **2019**, *133*, 106306. [[CrossRef](#)]
- Sigmund, O.; Maute, K. Topology optimization approaches: A comparative review. *Struct. Multidiscip. Optim.* **2013**, *48*, 1031–1055. [[CrossRef](#)]
- ANSYS® Academic Research Mechanical, Release 2020, Help System, Mechanical Analysis Guide; ANSYS, Inc: Canonsburg, PA, USA, 2020.
- Michael, S. ABAQUS/Standard User's Manual, Version 6.9; Dassault Systems: Vélizy-Villacoublay, France, 2009.
- Livermore Software Technology Corporation. *LS-Dyna Keyword User's Manual*; Livermore Software Technology: Livermore, CA, USA, 2014.
- Maheri, A. Multiobjective optimisation and integrated design of wind turbine blades using WTBM-ANSYS for high fidelity structural analysis. *Renew. Energy* **2020**, *145*, 814–834. [[CrossRef](#)]
- Zhou, Y.; Tian, K.; Xu, S.; Wang, B. Two-scale buckling topology optimization for grid-stiffened cylindrical shells. *Thin-Walled Struct.* **2020**, *151*, 106725. [[CrossRef](#)]
- Yan, X.; Bao, D.; Zhou, Y.; Xie, Y.; Cui, T. Detail control strategies for topology optimization in architectural design and development. *Front. Archit. Res.* **2021**, *11*, 340–356. [[CrossRef](#)]
- Shanmugasundar, G.; Dharanidharan, M.; Vishwa, D.; Kumar, A.P.S. Design, analysis and topology optimization of connecting rod. *Mater. Today Proc.* **2021**, *46*, 3430–3438. [[CrossRef](#)]
- Tian, X.; Sun, X.; Liu, G.; Deng, W.; Wang, H.; Li, Z.; Li, D. Optimization design of the jacket support structure for offshore wind turbine using topology optimization method. *Ocean Eng.* **2022**, *243*, 110084. [[CrossRef](#)]
- Tsavdaridis, K.D.; Nicolaou, A.; Mistry, A.D.; Efthymiou, E. Topology optimisation of lattice telecommunication tower and performance-based design considering wind and ice loads. *Structures* **2020**, *27*, 2379–2399. [[CrossRef](#)]
- He, L.; Gilbert, M.; Shepherd, P.; Ye, J.; Koronaki, A. A new conceptual design optimization tool for frame structures. In Proceedings of the IASS Annual Symposium: Creativity in Structural Design, Boston, MA, USA, 16–20 July 2018; MIT: Cambridge, MA, USA, 2018.
- Ye, J.; Shepherd, P.; He, L.; Gilbert, M.; Davison, B.; Tyas, A.; Gondzio, J.; Weldeyesus, A.; Fairclough, H. Computational layout design optimization of frame structures. In Proceedings of the IASS Annual Symposium, Hamburg, Germany, 25–28 September 2017.
- Weldeyesus, A.G.; Gondzio, J.; He, L.; Gilbert, M.; Shepherd, P.; Tyas, A. Adaptive solution of truss layout optimization problems with global stability constraints. *Struct. Multidiscip. Optim.* **2019**, *60*, 2093–2111. [[CrossRef](#)]
- Dorn, W.; Gomory, R.; Greenberg, H.J. Automatic design of optimal structures. *J. Mecanique* **1964**, *3*, 25–52.
- Met Office. *Dataset Collection Record: Met Office Integrated Data Archive System (MIDAS) Land and Marine Surface Stations Data (1853-Current)*; NCAS British Atmospheric Data Centre: Leeds, UK, 2021. Available online: catalogue.ceda.ac.uk (accessed on 10 December 2021).
- Martyn, S. *MIDAS Data User Guide for UK Land Observations; v20210705, Documentation*; Met Office: Exeter, UK, 2021. Available online: cedadocs.ceda.ac.uk/ (accessed on 9 December 2021).
- Turner, R.; Pirooz, A.A.S.; Flay, R.G.J.; Moore, S.; Revell, M. Use of High-Resolution Numerical Models and Statistical Approaches to Understand New Zealand Historical Wind Speed and Gust Climatologies. *J. Appl. Meteorol. Climatol.* **2019**, *58*, 1195–1218. [[CrossRef](#)]
- Miller, C.; Holmes, J.; Henderson, D.; Ginger, J.; Morrison, M. The Response of the Dines Anemometer to Gusts and Comparisons with Cup Anemometers. *J. Atmos. Ocean. Technol.* **2013**, *30*, 1320–1336. [[CrossRef](#)]
- Cook, J.N. *The Designer's Guide to Wind Loading of Building Structures. Part 1, Background, Damage Survey, Wind Data and Structural Classification*; Butterworths: London, UK, 1985.
- Lienhard, J.H. *Synopsis of Lift, Drag, and Vortex Frequency Data for Rigid Circular Cylinders*; Bulletin 300; Technical Extension Service, Washington State University: Washington, DC, USA, 1966.
- White, F.M. *Fluid Mechanics*, 5th ed.; McGraw-Hill: New York, NY, USA, 2003.
- EEN 1999-1-1; Eurocode 9: Design of Aluminium Structures—Part 1-1: General Structural Rules. The European Union Per Regulation 305/2011, Directive 98/34/EC, Directive 2004/18/EC; ICE Publishing: London, UK, 2007.

27. Majzoobi, G.H.; Freshteh-Saniee, F.; Khosroshahi, S.F.Z.; Mohammadloo, H.B. Determination of materials parameters under dynamic loading. Part I: Experiments and simulations. *Comput. Mater. Sci.* **2010**, *49*, 192–200. [[CrossRef](#)]
28. Wei, P.; Liu, Y.; Dai, J.G.; Li, Z.; Xu, Y. Structural design for modular integrated construction with parameterized level set-based topology optimization method. *Structures* **2021**, *31*, 1265–1277. [[CrossRef](#)]
29. Teimouri, M.; Mahbod, M.; Asgari, M. Topology-optimized hybrid solid-lattice structures for efficient mechanical performance. *Structures* **2021**, *29*, 549–560. [[CrossRef](#)]
30. Xiao, M.; Mukherjee, S.; Raghavan, B.; Dutta, S.; Breitkopf, P.; Zhang, W. Revisiting p-refinement in structural topology optimization. *Structures* **2021**, *34*, 3640–3646. [[CrossRef](#)]
31. Luo, Z.; Yang, J.; Chen, L. A new procedure for aerodynamic missile designs using topological optimization approach of continuum structures. *Aerosp. Sci. Technol.* **2006**, *10*, 364–373. [[CrossRef](#)]
32. Youn, S.K.; Park, S.H. A study on the shape extraction process in the structural topology optimization using homogenized material. *Comput. Struct.* **1997**, *62*, 527–538. [[CrossRef](#)]
33. Yang, R.J.; Chuang, C.H. Optimal topology design using linear programming. *Comput. Struct.* **1994**, *52*, 265–275. [[CrossRef](#)]
34. Martin, A.; Deierlein, G.G. Structural topology optimization of tall buildings for dynamic seismic excitation using modal decomposition. *Eng. Struct.* **2020**, *216*, 110717. [[CrossRef](#)]
35. CAP 437; Standards for Offshore Helicopter Landing Areas. Civil Aviation Authority: London, UK, 2021.
36. Riks, E. The Application of Newton's Method to the Problem of Elastic Stability. *J. Appl. Mech.* **1972**, *39*, 1060–1065. [[CrossRef](#)]
37. Zhao, Y.; Zhai, X.; Wang, J. Buckling behaviors and ultimate strengths of 6082-T6 aluminum alloy columns under eccentric compression—Part I: Experiments and finite element modeling. *Thin-Walled Struct.* **2019**, *143*, 106207. [[CrossRef](#)]
38. Riks, E. An incremental approach to the solution of snapping and buckling problems. *Int. J. Solids Struct.* **1979**, *15*, 529–551. [[CrossRef](#)]
39. Kwon, D.; Kareem, A. NatHaz On-Line Wind Simulator (NOWS): Simulation of Gaussian Multivariate Wind Fields. NatHaz Modeling Laboratory Report. 2006. Available online: windsim.ce.nd.edu/ (accessed on 20 December 2021).
40. Kwon, D.K.; Kareem, A. A framework for gust-front factor in Conference. In Proceedings of the 11th Americas Conference on Wind Engineering (ACWE 11), San Juan, Puerto Rico, 22–26 June 2009.
41. Juang, J.N.; Pappa, R.S. An eigensystem realization algorithm for modal parameter identification and model reduction. *J. Guid. Control. Dyn.* **2012**, *8*, 620–627. [[CrossRef](#)]
42. Ottersböck, M.J.; Leitner, M.; Stoschka, M. Characterisation of actual weld geometry and stress concentration of butt welds exhibiting local undercuts. *Eng. Struct.* **2021**, *240*, 112266. [[CrossRef](#)]
43. Pandey, M.; Young, B. Experimental investigation on stress concentration factors of cold-formed high strength steel tubular X-joints. *Eng. Struct.* **2021**, *243*, 112408. [[CrossRef](#)]
44. Feng, R.; Tang, C.; Chen, Z.; Roy, K.; Chen, B.; Lim, J.B.P. A numerical study and proposed design rules for stress concentration factors of stainless steel hybrid tubular K-joints. *Eng. Struct.* **2021**, *233*, 111916. [[CrossRef](#)]
45. Godio, M.; Portal, N.W.; Flansbjerg, M.; Magnusson, J.; Byggnevi, M. Experimental and numerical approaches to investigate the out-of-plane response of unreinforced masonry walls subjected to free far-field blasts. *Eng. Struct.* **2021**, *239*, 112328. [[CrossRef](#)]
46. Aursand, E.; Dumoulin, S.; Hammer, M.; Lange, H.I.; Morin, A.; Munkejord, S.T.; Nordhagen, H.O. Fracture propagation control in CO₂ pipelines: Validation of a coupled fluid-structure model. *Eng. Struct.* **2016**, *123*, 192–212. [[CrossRef](#)]
47. Bergmeister, K.; Brunello, P.; Pachera, M.; Pesavento, F.A. Schrefler, Simulation of fire and structural response in the Brenner Base Tunnel by means of a combined approach: A case study. *Eng. Struct.* **2020**, *211*, 110319. [[CrossRef](#)]